Recent ground thermo-hydrological changes in a Southern Tibetan endorheic catchment and implications for lake level changes

Léo C.P. Martin[1,2,3], Sebastian Westermann[2,4], Michele Magni[1], Fanny Brun[1,5], Joel Fiddes[6], Yanbin Lei[7,8], Philip Kraaijenbrink[1], Tamara Mathys[9], Moritz Langer[10,11], Simon Allen[12] and Walter W. Immerzeel[1]

1. Faculty of Geosciences, Utrecht University, Utrecht, The Netherlands
2. Department of Geosciences, University of Oslo, Blindern, 0316 Oslo, Norway
3. Aix Marseille Univ, CNRS, IRD, INRAE, CEREGE, Aix-en-Provence, France
4. Center for Biogeochemistry in the Anthropocene, Oslo, Norway
5. Université Grenoble Alpes, CNRS, IRD, Grenoble INP, IGE, Grenoble, France
6. WSL Institute for Snow and Avalanche Research SLF, Davos, Switzerland
7. Key Laboratory of Tibetan Environment Changes and Land Surface Processes, Institute of Tibetan Plateau Research, Chinese Academy of Sciences, Beijing 100101, China
8. CAS Center for Excellence in Tibetan Plateau Earth System Sciences, Beijing 100101, China
9. Department of Geosciences, University of Fribourg, Fribourg, Switzerland
10. Alfred Wegener Institute Helmholtz Centre for Polar and Marine Research, 14473 Potsdam, Germany
11. Department of Geography, Humboldt Universität zu Berlin, 12489 Berlin, Germany
12. Department of Geography, University of Zurich, Zürich, Switzerland

Correspondence to: Léo Martin   (leo.doug.martin@gmail.com)
                       Walter Immerzeel   (w.w.immerzeel@uu.nl)

Abstract: 418 words
Main: 13,364 words, 11 figures, 2 tables
Appendices: 446 words, 3 figures, 1 table

Abstract

Climate change modifies the water and energy fluxes between the atmosphere and the surface in mountainous regions such as the Qinghai-Tibet Plateau (QTP), which has shown substantial hydrological changes over the last decades, including rapid lake level variations. The ground across the QTP hosts either permafrost or seasonally frozen and, in this environment, the ground thermal regime influences liquid water availability, evaporation and runoff. Therefore, climate-driven modifications of the ground thermal regime may contribute to lake level variations, yet this hypothesis has been relatively overlooked until now.

This study focuses on the cryo-hydrology of the catchment of Lake Paiku (Southern Tibet) for the 1980-2019 period. We use TopoSCALE and TopoSUB to downscale ERA5 data, in an effort to account for the spatial variability of the climate in our forcing data. We use a distributed setup of the CryoGrid community model (version 1.0) to quantify thermo-hydrological changes in the ground during this period. Forcing data and simulation outputs are validated with data from a weather station, surface temperature loggers and observations of lake level variations. Our lake budget reconstruction shows that the main water input to the lake is direct precipitation (310 mm per year), followed by glacier runoff (280 mm per year) and land runoff (180 mm per year). However, altogether these components do not offset evaporation (860 mm per year).

Our results show that both seasonal frozen ground and permafrost have warmed (0.17 °C per decade 2 m deep), increasing the availability of liquid water in the ground and the duration of seasonal thaw. Correlations with annual values suggest that both phenomena promote evaporation and runoff. Yet, ground warming drives a strong increase in subsurface runoff, so that the runoff/(evaporation + runoff) ratio increases over time. This increase likely contributed to stabilizing the lake level decrease after 2010.

Summer evaporation is an important energy sink and we find active layer deepening only where evaporation is limited. The presence of permafrost is found to promote evaporation at the expense of runoff, consistent with recent studies suggesting that a shallow active layer maintains higher water contents close to the surface. However, this relationship seems to be climate-dependent and we show that a colder and wetter climate produces the opposite effect. Although the present study was performed at catchment scale, we suggest that this ambivalent influence of permafrost may help to understand the contrasting lake level variations observed between the South and North of the QTP, opening new perspectives for future investigations.

Main text

1. Introduction

Climate change is amplified in mountainous environments, with major consequences for ecosystems, landscapes, hydrology, human communities and infrastructure (IPCC, 2019). Station observations show that global warming is elevation dependent, with the strongest warming rates being observed at high elevations (Pepin et al., 2015; Wang et al., 2014). Over the Qinghai-Tibet Plateau (QTP), a significant increase in surface air temperatures has been recorded since the 1980s, in particular in the North of the plateau (Zhang et al., 2022). This has been accompanied by a decrease in wind speed, humidification of the air, and a general increase in precipitation, although with a strong spatial variability (Bibi et al., 2018). Altogether, these changes have affected the surface energy balance of the plateau through a shift of the Bowen ratio towards more latent heat fluxes, limiting the sensible surface warming (Yang et al., 2014a).

These changes in water and energy fluxes between the atmosphere and the surface have the potential to alter the hydrological cycle of the QTP, which is the headwater region for major Asian rivers. As such, increasing trends of evaporation over land have been measured (3.8 mm per decade since the 1960s) with strong spatial variability both in absolute values and increase rates (Wang et al., 2020b). Changes in the seasonality of river discharge (Cao et al., 2006) and groundwater discharge (Niu et al., 2011) were reported for the same period. Overall glacier shrinkage has also been observed since the 1960s with a persistent increase in glacier mass loss rates (Bhattacharya et al., 2021; Hugonnet et al., 2021).

The QTP also features more than 1,000 lakes larger than 1 km^2 (Zhang et al., 2017), most of them located in endorheic catchments. Lake volume changes are therefore attributable to climatic and hydrological changes occurring within the lake catchment, such as glacier melt, ground ice melt, precipitation, evaporation or runoff patterns. The majority of these lakes have experienced a pronounced increase in water levels since the 1990s (Lei et al., 2013, 2014), a trend that was suggested to be mainly driven by changes in precipitation and evaporation patterns (Yao et al., 2018) rather than by an increase

in glacier mass loss and runoff (Brun et al., 2020; Zhang et al., 2021a). Nevertheless, lake level variations are not uniform across the QTP and exhibit important spatial variability. Whereas the northern and central QTP have recorded lake expansion, the southern parts of the plateau have experienced lake shrinkage (Qiao et al., 2019; Zhang et al., 2021a, 2020a). Such a complex pattern challenges our understanding of the hydrological changes occurring in these high Asian watersheds.

In this regard, new insights on hydroclimatic changes over the QTP can emerge from the investigation of the coupled energy and water fluxes between the ground surface/subsurface and the atmospheric boundary layer. These fluxes are driven by the climate and have a major impact on cold-region hydrology (Pomeroy et al., 2007; Gao et al., 2021; Bring et al., 2016). Indeed, hydrological variables (precipitation, evaporation, runoff) affect the soil water content, which changes its thermal properties, the distribution between latent and sensible fluxes and thus substantially influences the ground thermal regime (Bring et al., 2016; Koren et al., 1999; Martin et al., 2019). In turn, the ground thermal regime modifies the relative proportion of frozen and liquid subsurface water, influencing infiltration possibilities and the amount of water available for evaporation and surface/subsurface runoff (Yi et al., 2006; Carey and Woo, 2001).

So far, climate induced thermo-hydrological changes over the QTP have received limited attention. Large-scale modeling studies reported changes in the seasonal ground freezing cycles characterized by a reduction of the frost depth and duration of the frozen period since the 1960s (Qin et al., 2018; Wang et al., 2020a) and notable ground warming trends in summer and winter (Qin et al., 2021). Similar ground warming trends were reported in the regional modeling study from Qin et al. (2017), along with an increasing trend in evaporation and a decrease of the runoff coefficient over time. Plateau-scale surface energy balance modeling from Wang et al. (2020b) reported that increasing trends in evapotranspiration could be mainly explained by variations in air temperature and net radiation at the surface.

Complementary to seasonally frozen ground, permafrost is also a distinctive feature of climate-surface interactions in cold regions. Large-scale permafrost modeling suggests that it covers a significant part of the QTP, mainly as continuous permafrost in the north of the plateau and as discontinuous or sporadic in the south (Obu et al., 2019). Permafrost on the QTP usually has a low ice

83 content due to limited precipitation and strong evaporation (Wu et al., 2005; Yang et al., 2010).

84 Borehole temperature measurements show that it is a relatively warm type of permafrost (Biskaborn et

85 al., 2019; Wu and Zhang, 2008) and its exposure to high solar radiations makes it sensitive to changes

86 in surface conditions and climate change (Yang et al., 2010). Since the 1960s, climate change has driven

87 permafrost warming across the plateau (Ran et al., 2018; Shaoling et al., 2000). Ran et al. (2018) reports

88 that most of the plateau exhibits a warming trend of the ground comprised between 0.26 and 0.74 C

89 per decade and half of the plateau warms at a rate higher than 0.5 °C per decade. This warming is

90 accompanied by upward migration (of around 100 m between the 1960s and 2000s) and shrinkage of

91 permafrost covered areas (24% of the permafrost extent lost between the 1960s and the 2000s, Ran et

92 al., 2018).

93   Permafrost grounds are characterized by a strong interplay between the ground thermal regime and

94 the land hydrology. Seasonal thawing and freezing of the active layer are driven by the surface energy

95 balance which, in return, influences surface and subsurface runoff (Kurylyk et al., 2014; Walvoord and

96 Kurylyk, 2016; Sjöberg et al., 2021) and evaporation (Gao et al., 2021). In this regard, both large-scale

97 and regional modeling indicate that thawing permafrost enhances evapotranspiration (Qin et al., 2017;

98 Wang et al., 2020b). Qin et al. (2017) also report that the increase in evaporation is logically

99 concomitant with a decrease in the runoff coefficient. Additionally, permafrost stores water as ground

100 ice and its thawing can trigger the release of liquid water in the watershed, contributing up to 15% of

101 the annual river streamflow (Cheng and Jin, 2013; Yang et al., 2019).

102   These hydrological changes are tied to various interdependent climate-driven physical processes

103 happening at the ground surface and subsurface (e.g. surface energy balance, infiltration, water phase

104 change, heat conduction…). Because these processes exhibit a strong spatial variability in high mountain

105 environments, it is challenging to represent them accurately together on large spatial scales. Therefore,

106 a deeper understanding of the impact of ground thermo-hydrological changes on the High Asia water

107 cycle can be gained through small-scale physical modeling of these processes. Yet, for now, physics-

108 based approaches at the catchment scale aiming to connect the ground thermo-hydrological regime and

109 the observed hydrological changes on the QTP (such as lake level changes) remain scarce. They are

110 however a powerful approach to tackle the question: how much might climate-driven ground thermal

changes affect the water cycle in high mountain headwater regions? In this study, we use physical land surface modeling to quantify the ground thermo-hydrological changes in an endorheic Tibetan catchment over the last 40 years as a response to climate change. We show the interplay in the water and energy fluxes occurring between the atmosphere, the surface and the subsurface and discuss their impact on the hydrology of the catchment and their implication regarding lake level variations.

2. Study area: the Paiku catchment

The Paiku catchment is located in south-western Tibet, China, close to the border with Nepal (28.8°N - 85.6°E, Fig. 1). Its southern edge lies 7 km from the Shishapangma peak (8027 masl). The catchment is endorheic and spans over 78 km from North to South, 66 km from East to West and covers 2 400 km^2. The median elevation of the catchment is 4872 masl, ranging from 7272 masl to its lowest point, lake Paiku at 4580 masl. Geologically, the catchment is mainly located in the Tethys Himalayan, and thus, an important part of the formations underlying the catchment are metamorphized sedimentary series (Appendix B, Fig. B1). The southern part of the catchment crosses the Southern Tibetan Detachment, and thus, the southern ridges of the massif belong to the High Himalayan metamorphic formations in the west and to the High Himalayan leucogranites of the Shishapangma massif on the east. The north and north-east ridges are formed by granite intrusions surrounded by metamorphic domes. The inner part of the catchment presents Plio-Quaternary formations such as alluvial fans close to the ridges and inclined alluvial plains in its inner parts (Aoya et al., 2005; Searle et al., 1997; Wünnemann et al., 2015).

Automatic Weather Station (AWS) observations (5033 masl, Oct 2019 – Sept 2021, Fig. 1) show that the climate in the catchment is characterized by a relatively small temperature amplitude during the year (around 20 °C, JJA being the warmest months and DJF the coldest) and significant daily amplitude (up to 10 °C during the warm season). The mean annual temperature is -1.5 °C at the AWS, where night freezing can occur until the beginning of June and resume at the beginning of October. The catchment is dry (200-300 mm year^{-1}) and precipitation mostly falls as rain during the monsoon (JJAS).

Around 5% of the catchment is covered by glaciers (RGI Consortium, 2017), which are concentrated in its southwestern part. They feed several proglacial lakes that can reach up to 6 km in length. Geodetic glacier mass budgets show that, similar to other glaciers in the region, glaciers of the Paiku catchment have undergone sustained mass loss at least since the 1970s, with an average mass balance of -0.3 m w.e.a^{-1} until the beginning of the 2000s and around -0.4 m w.e.a^{-1} thereafter (Bhattacharya et al., 2021). There are more than 10 rivers that drain the catchment towards the lake and most of them only exhibit a seasonal activity during the monsoon months. The three main ones are

143 (Fig. 1), Daqu (glacier-fed, 450 km^2), Bulaqu (glacier-fed, 325 km^2) and Barixiongqu (non-glacier-fed,

144 703 km^2, Lei et al., 2018).

145 In the north-west of the catchment, Lake Paiku covers approx. 280 km^2 (11.5% of the catchment

146 surface area) and spans over 27 km from North to South. It has a mean water depth of 41 m, with a

147 maximum water depth of 73 m (Lei et al., 2018). It receives water from direct precipitation and from

148 land and glacier runoff which can be routed at the surface via the river systems or the subsurface via

149 the alluvial formations. Because it is hydrologically closed, the lake mainly loses water through

150 evaporation. Previous studies reported lake level fluctuations over different time scales. It reached 4665

151 masl (85 m higher than the present level) prior to 25 ka BP and at the onset of the Holocene (11.9-9.5

152 ka BP), afterwards, the lake shrank gradually (Wünnemann et al., 2015). More recently, the lake level

153 decreased by 3.7 m between 1972 and 2015, losing 4.2% of its surface and 8.5% of its volume.

154 Measurements have been performed since the end of the 1970s and allow to accurately know the

155 evolution of the lake level until today (Lei et al., 2021, 2018), they are used in this study to validate our

156 hydrological results (Sect 3.2.1, Fig. 5D and 6B). At the seasonal scale, the lake level cycle has an

157 amplitude of ~ 0.4 m. It is marked by a strong increase during the monsoon period (JJAS) supported by

158 direct precipitation, glacier melt and land runoff. From October and until the next monsoon period,

159 evaporation dominates the lake mass budget and the level decreases rapidly until January and at a slower

160 rate afterwards (Lei et al., 2021).
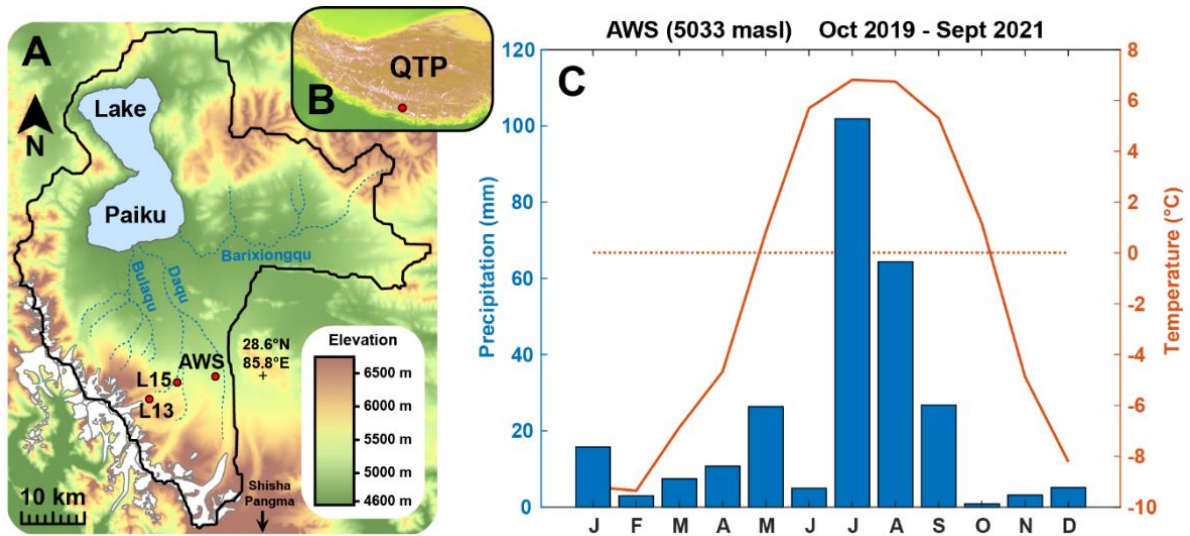
161
162 *Figure 1. The Paiku Catchment. A: Topographic and hydrologic map of the catchment with the glaciers*
163 *in white, the ephemeral rivers in dark blue and the lake in light blue (elevation: SRTM data courtesy of*
164 *the U.S. Geological Survey). AWS: Automatic Weather Station. L13 and L15 are surface temperature*
165 *loggers (Sect. 3.1). B: Localization of the catchment over the QTP. C: Monthly temperature and*
166 *precipitation recorded at the AWS between October 2019 and September 2021.*

3. Material and methods

3.1.   Field measurements

An AWS was set up in October 2019 in the South of the catchment at an elevation of 5033 masl (Fig. 1). It is equipped with various sensors which record air temperature, pressure, relative humidity, wind speed, incoming and outgoing long and short wave radiations and precipitation every 15 minutes. The meteorological record extends to September 2021 and covers a period of nearly 2 years. We used it to evaluate and correct the distributed downscaled climatic forcing on which we rely in our modeling framework (Sect. 3.2.2.).

Two temperature loggers recorded the surface temperature in the vicinity of the AWS location. Logger 15 (L15) is located at 5055 masl, 6 km west of the AWS. Logger 13 (L13) is located at 5356 masl, 12 km west of the AWS (Fig. 1). Both loggers were buried 10 to 15 cm below the surface to avoid direct solar radiation on the sensors and recorded surface temperature at a 20-minute timestep from October 2017 to October 2018. These surface temperature records were used to evaluate the simulations (Sect. 3.2.4.).

3.2.   Catchment thermo-hydrological modeling

3.2.1. *Conceptual hydrological model for the catchment*

To understand the level variations of lake Paiku over the last 40 years (1980-2019 period), we develop an approach at the catchment scale. Because the catchment is hydrologically closed, the lake receives water input via direct precipitation, land surface and subsurface runoff, and glacier runoff. Conversely, it loses mass via evaporation. Because the quantification of water flows between the lake and potential aquifers surrounding it is difficult (Rosenberry et al., 2015), our approach assumes that these flows are negligible. The present study requires quantification of the different terms of the hydrological balance. Under these assumptions, the hydrological balance of the lake is given by the following equation:

191          $\Delta z_{Lake} = Precipitation_{Lake} + Runoff_{Land} + Runoff_{Glacier} - Evaporation_{Lake}$

192   The production of forcing data for the catchment (including precipitation) is detailed in Sect. 3.2.2.

193 The land hydrology processes are quantified using the CryoGrid community model (version 1.0)

194 (Westermann et al., 2023) as described in section 3.2.3. Distributed 1D simulations are used to quantify

195 land evaporation and runoff. The routing of water in the catchment is not represented and the runoff

196 computed for a given simulation is directly accounted as a water input for the lake. The evaporation

197 from the lake is simulated using the CryoGrid3-Flake model (Langer et al., 2016) as described in

198 Section 3.2.5. Glacier melt is not modeled, but estimated for the study period (1980-2019) from remote

199 sensing observations. From these observations, glacier yield is calculated as described in Sect. 3.2.6.

200 Our catchment-scale approach to represent the hydrological balance of the lake is summarized in Fig. 2.

201 Based on this approach, we can evaluate the performance of our framework (Sect. 4.1.2), by comparing

202 the simulated lake balance with the one derived from the detailed observations of lake level variations

203 over the study period (Lei et al., 2018, 2021).
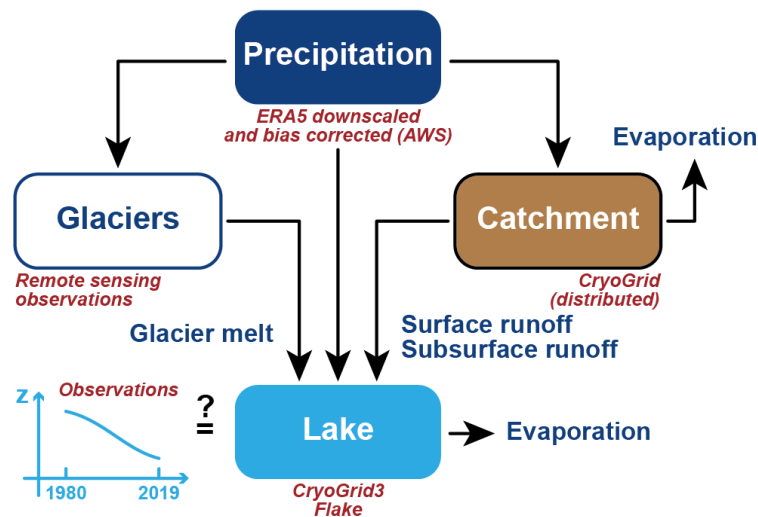
204
205   *Figure 2. Conceptual hydrological framework for the study.*
206

207   *3.2.2. Forcing data production and validation*

208   In high mountain environments, topography creates strong spatial variability of temperature and

209 incoming radiation, which impact the surface energy balance (Klok and Oerlemans, 2002) and the

210 ground thermo-hydrological regime (Magnin et al., 2017). Our approach requires forcing data that (i)

211 captures this variability, (ii) includes numerous variables such as air temperature, incoming long and

212 short wave radiations, wind speed, specific humidity, rain and snowfall and (iii) covers the 40 years

213   study period at a sub-daily timestep. The TopoSCALE approach (Fiddes and Gruber, 2014) was

214   developed for this purpose and allows to downscale reanalysis products like ERA5 (Hersbach et al.,

215   2020) at high resolution (here ~ 100 x 100 m).

216   Additionally, because working at a 10^{-2} km^2 spatial resolution over a 2400 km^2 catchment would

217   require more than 200,000 forcing files and simulations, we rely on the TopoSUB method (Fiddes and

218   Gruber, 2012) to reduce computational costs. This method uses a SRTM30 Digital Elevation Model to

219   explore redundancies in physiographic parameters of the study area such as elevation, aspect, slope and

220   sky-view factor and to identify groups of high-resolution pixels (100 x 100 m) sharing similar values

221   for these parameters. From there, all the high-resolution pixels belonging to such a group are only

222   described as a single TopoSUB point, for which climatic variables can be downscaled to create one

223   single dataset of climatic timeseries. The degree of similarity required by TopoSUB to identify groups

224   of high-resolution pixels with redundant physiographic parameters can be adjusted by choosing the final

225   number of TopoSUB points (and thus climate datasets) that should be used to cover the area

226   corresponding to one ERA5 pixel. The Paiku catchment intersects 8 ERA5 pixels at 30 km resolution

227   and we chose to use 50 TopoSUB points within each ERA5 pixel to cover the spatial variability created

228   by the topography on small-scale climate. Ultimately, 368 TopoSUB points are used to cover the

229   catchment. The average level of redundancy (i.e. the average number of high-resolution pixels

230   represented by a single TopoSUB point) is 723 ± 745 (1σ, median: 506, min: 1, max: 4347). Appendix

231   C, Fig. C1 shows the distribution of the TopoSUB points and a reconstruction of the topography of the

232   catchment based on this approach. The period covered by the forcing datasets starts on 1st January 1980

233   and ends on 31st August 2020 (40 years and 8 months).

234   In the TopoSCALE statistical downscaling approach, we do not rely on the AWS data and thus the

235   downscaled ERA5 data can be biased, as is often the case over Asia (Jiang et al., 2021, 2020; Jiao et

236   al., 2021; Orsolini et al., 2019). Comparison against the available AWS observations (Appendix D, Fig.

237   D1) indeed highlights notable differences in variables such as air temperature and precipitation. From

238   these differences, we derived monthly bias correction factors that we applied systematically to all of the

239   368 climate forcing datasets. The catchment averages for precipitation and air temperatures are shown

240   in Fig. 3. In this figure and across the rest of the study, we use p-values to evaluate the significance of

241 linear trends in the temporal evolution of certain variables (temperature, precipitation, evaporation…).

242 This p-value tests the null hypothesis which supposes that the value of the slope is equal to zero. The

243 hypothesis is tested using the Student's t-test, by comparing the distance between the estimated slope

244 and 0, relative to the standard error of the slope. We did not report trends when this p-value (probability

245 of a null slope) was higher than 0.005.
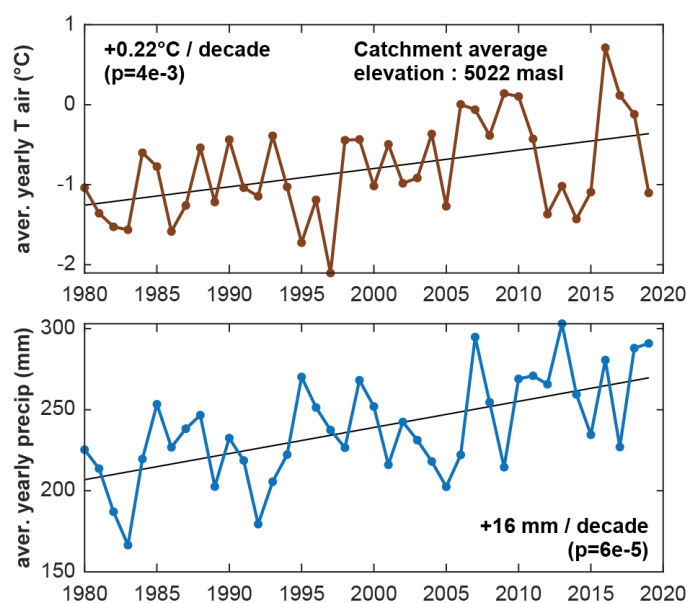
246
247 *Figure 3. Climate forcing data for the land and lake modeling. Annual catchment-average air*
248 *temperature (2 m above ground) and annual total precipitation for the study period. Note that the model*
249 *is also forced by incoming short and long wave radiations, humidity, windspeed and air pressure.*
250 *Details about the spatial and temporal resolution of the distributed forcing data are presented in Sect.*
251 *3.2.2.*
252

253 ### 3.2.3. The CryoGrid community model (version 1.0)

254 To simulate the ground thermo-hydrological regime, we use the CryoGrid community model

255 (Westermann et al., 2023). The CryoGrid community model (CG) is a land surface model designed for

256 applications in cold regions where seasonal frozen ground or permafrost may occur. The model

257 implements heat transfer in a 1D soil column, accounting for freeze-thaw processes of soil water using

258 effective heat capacity (Nakano and Brown, 1972). To do so, soil freezing curves are based on

259 Dall'Amico et al. (2011) as detailed in (Westermann et al., 2013). Vertical water movement in the soil

260 column is based on Richards equation (Richardson, 1922; Richards, 1931). The soil matric potential

261 and hydraulic conductivity follow van Genuchten, (1980) and Mualem (1976). Additionally, to

262 represent the obstruction of connected porosity by ice formation, the hydraulic conductivity is reduced

263 by a factor dependent on the local ice content, following Dall'Amico et al. (2011). The model features

264 the snowpack module called *CG Crocus* described in Zweigel et al. (2021) that adapts the snow physics

265 parameterizations from the CROCUS scheme (Vionnet et al., 2012) to the native snow module of

266 CryoGrid3 (Westermann et al., 2016). At the surface, the model uses a surface energy balance module

267 to calculate the ground surface temperature and water content. The turbulent fluxes of sensible and

268 latent heat are calculated using a Monin–Obukhov approach (Monin and Obukhov, 1954). Evaporation

269 is derived from the latent heat fluxes using the latent heat of evaporation and is adjusted to the available

270 water in the soil. It occurs in the first grid cell only, but water can be drawn upwards due to matric

271 potential differences. Because vegetation is very scarce in the catchment, we do not expect transpiration

272 to have a strong imprint on evapotranspiration and our calculations do not unravel evaporation from

273 transpiration.

274   *3.2.4. Model setup and validation*

275   The setup of the CryoGrid community model for the land is presented in Fig. 4. To capture the

276 high spatial variability of mountainous climate, our approach relies on the 368 climate forcing datasets

277 to cover the catchment (see section 3.2.2). This approach enables us to perform spatially distributed

278 modeling. All of the 368 simulations are independent and use the same parameterization. In absence of

279 direct observation of the soil stratigraphy within the catchment, the soil column was designed to agree

280 with field observations in the region (Yuan et al., 2020; Wang et al., 2009; Hu et al., 2020; Luo et al.,

281 2020; Yang et al., 2014b; Wang et al., 2008), to be consistent with similar modeling approaches across

282 Tibet (Chen et al., 2018; Song et al., 2020) and to be consistent with input datasets (Shangguan et al.,

283 2013, 2017). Thus, the soil stratigraphy is divided into 3 units: a top soil (0.3 m thick), a bottom soil

284 (1.7 m thick), and a bedrock unit (extending beyond the depth of interest of the study). An overview of

285 the parameters for each unit, their source and the way they are calculated is presented in Appendix A,

286 Tab. A1.

287   Regarding the processes implemented in the model (Sect. 3.2.3), infiltration according to Richards

288 equation only occurs in the top and bottom soil units. The bedrock unit has a static water content.

289 Unraveling surface from subsurface flow is an ongoing challenge in catchment-scale hydrology

290 (McDonnell, 2013) and this distinction is important in mountain terrains where these two flows can

291 behave differently due to the complex topography (Seibert et al., 2003; Gao et al., 2014; Hu et al.,

292   2020). For this study, we rely on a simple approach that is based on thresholds regarding the soil water

293   content (porosity and field capacity). This kind of approaches are thus based on soil properties and have

294   often been used in hydrological modeling studies (Vörösmarty et al., 1989; Shaman et al., 2002;

295   Kelleners et al., 2010; Kampf, 2011; Samuel et al., 2008). In detail, we compute surface and subsurface

296   flow as follows.

297   On the one hand, surface runoff is computed relative to the saturation level of the soil column.

298   When the entire soil column is saturated (WC = porosity), additional water input from precipitation or

299   snowmelt is directly counted as surface runoff. On the other hand, subsurface runoff is computed

300   relative to the field capacity of the ground, which is an input parameter of the model. When the water

301   content (WC) of a ground cell exceeds this field capacity (FC), the amount of water corresponding to

302   WC-FC is available to produce subsurface runoff. We use the lateral boundary condition

303   LAT_WATER_RESERVOIR from the CryoGrid community model (Westermann et al., 2023) to

304   account for this subsurface runoff. The speed at which this available water exits the soil column towards

305   the lake is calculated with Darcy's law, using the hydrological conductivity of the ground and the mean

306   slope of the catchment as hydraulic slope.

307   Because we do not have knowledge of the distributed thermal state with depth over the catchment

308   at the beginning of the simulations, we assume temperature profiles were in equilibrium with the climate

309   of the 5 first years of modeling (1980-1984). To do so, we start our simulations with a 60-year spin-up

310   of these first 5 years (12 repetitions), which is sufficient to establish a stable temperature profile over

311   the first 9 to 80 meters depending on the simulations, extending beyond the hydrologically active part

312   of the ground (the first 2 meters).
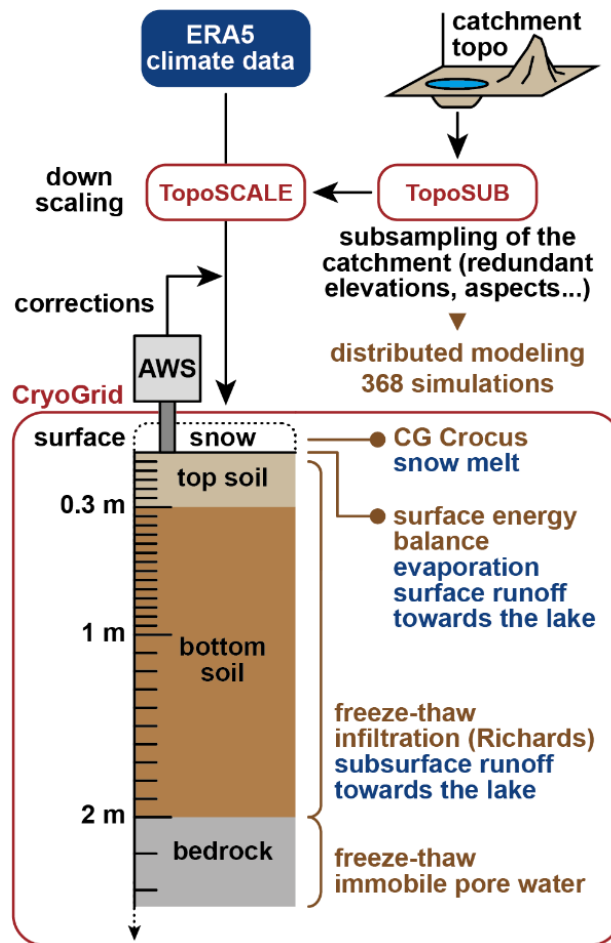
313
314 *Figure 4. Modeling framework for the land hydrology. ERA5 data are downscaled using the TopoSUB*
315 *and TopoSCALE approaches (Fiddes and Gruber, 2014, 2012). The downscaled data are bias-*
316 *corrected based on the AWS observations. Distributed 1D simulations are performed using the*
317 *CryoGrid community model (Westermann et al., 2023). The vertical resolution is indicated with the tick*
318 *marks on the depth axis.*
319
320 To validate model simulations, the simulated ground surface temperatures (GST) are compared to

321 the two temperature logger time series acquired in the vicinity of the AWS (Sect. 3.1). We used this

322 comparison to calibrate the surface roughness used for the surface energy balance calculations in the

323 model.

324 The following method is used to produce area-averaged evaporation and runoff (in mm water

325 equivalent) in a zone of interest. For a given TopoSUB point in this zone, the model produces

326 hydrological values in m^3 using the area of a TopoSUB pixel on the catchment map. Then these values

327 are multiplied by the number of pixels in the zone corresponding to this TopoSUB point in particular,

328 and this for all the relevant TopoSUB points covering the zone (e.g. evaporation in warm permafrost).

329 Then the area of interest is calculated by counting the number of pixels in the zone of interest and

330   multiplying this number by the area of a pixel. Then the total volume is divided by the total surface for

331   the zone of interest to obtain the final value in mm.

332   *3.2.5. Lake modeling*

333   The lake thermo-hydrological response to the climatic forcing data is simulated using the

334   CryoGrid3-Flake model (Langer et al., 2016). The two models were coupled by Langer et al. (2016) to

335   simulate the thermal regime of thermokarst lakes (including surficial water freezing and melting) and

336   underlying ground. Here we use the coupled models mainly to quantify evaporation at the lake surface.

337   In the coupled model, the native surface energy balance module of CryoGrid3 (Westermann et al., 2016)

338   was amended to account for processes tied to free water surface energy balance: (i) the dependence of

339   the albedo of a water surface to solar angle (and thus time of the day) and wind speed (and wave

340   formation), (ii) the dependence of the surface roughness length to wind speed (and wave formation) and

341   (iii) the exponential decay of incoming radiation with depth in the water column. Similar to the land

342   simulations, the lake simulations were forced by the downscaled ERA5 data (with the TopoSUB and

343   TopoSCALE methodology), with the corrections derived from the AWS data (Sect. 3.2.2). The

344   simulations were initiated with a 20-year spin-up of the 1980-1984 climate. The simulation results

345   corresponding to the four ERA5 tiles covering the lake were then averaged using the respective spatial

346   footprint of each tile on the lake.

347   *3.2.6. Quantification of glacier mass change*

348   Multiple studies quantified the volume change of the glaciers located within the Paiku catchment

349   in the recent past (1970s to 2020). To our knowledge, there are no field based measurements of glacier

350   mass balance available in this catchment. As a consequence, we rely solely on geodetic mass balance

351   studies (Brun et al., 2017; Maurer et al., 2019; King et al., 2019; Shean et al., 2020; Hugonnet et al.,

352   2021). All these studies estimated glacier volume changes over periods of 20-30 years from satellite

353   derived DEMs. As a consequence, we can only estimate the average annual glacier mass balance, and

354   not the year-to-year variability. Glaciers occupy approximately 113 km^2 in the Paiku catchment. They

355   have shrunk for the past fifty years at a rate of 0.44 % y^{-1}, from an area of 132 km^2 in 1975 to 122 km^2

356   around 2000 and to their current extent (King et al., 2019; Bolch et al., 2019). The average mass

357   balances for the period 1975-2000 and 2000-2020 are -3.9 $\pm$ 2.1$\times10^{10}$ kg y^{-1} and -5.4 $\pm$ 2.4$\times10^{10}$ kg y^{-1},

358   respectively (-4.6 $\pm$ 2.5 10^7 m^3 and -6.4 $\pm$ 2.8 10^7 m^3 with a 850 kg m^{-3} density). These mass balances

359   correspond to specific mass balances of -0.31 $\pm$ 0.17 m of water equivalent per year (w.e. y^{-1}) and -0.47

360   $\pm$ 0.21 m w.e. y^{-1}, respectively.

361   Regarding glacial runoff, it was estimated to 320 $\pm$ 4 mm per year for the 2001-2010 period by

362   Biskop et al. (2016) using a temperature-index approach for ice melt. For the 2000-2018 period, Zhang

363   et al. (2020b) derived a runoff value of 52 $\pm$ 12 mm per year (1.24 $\pm$ 0.29 10^8 m^3 per year that we scaled

364   to the basin area). The value we derive of 39 $\pm$ 13 mm per year thus finds good consistency with the

365   latter one (Sect. 4.1).

4. Results

4.1.   Model validation and hydrological budget of Lake Paiku

4.1.1. Model validation

Simulated daily ground surface temperatures are in good agreement with the observed ones, showing a bias of -0.2 °C and 0.6 °C and a RMSE of 1.4 °C and 1.6 °C for loggers 15 and 13, respectively (Fig. 5A and 5C). Most of this RMSE is explained by a mismatch between model and observations in the tails of the temperature distribution, whereas intermediate temperatures exhibit the best agreement with observations.
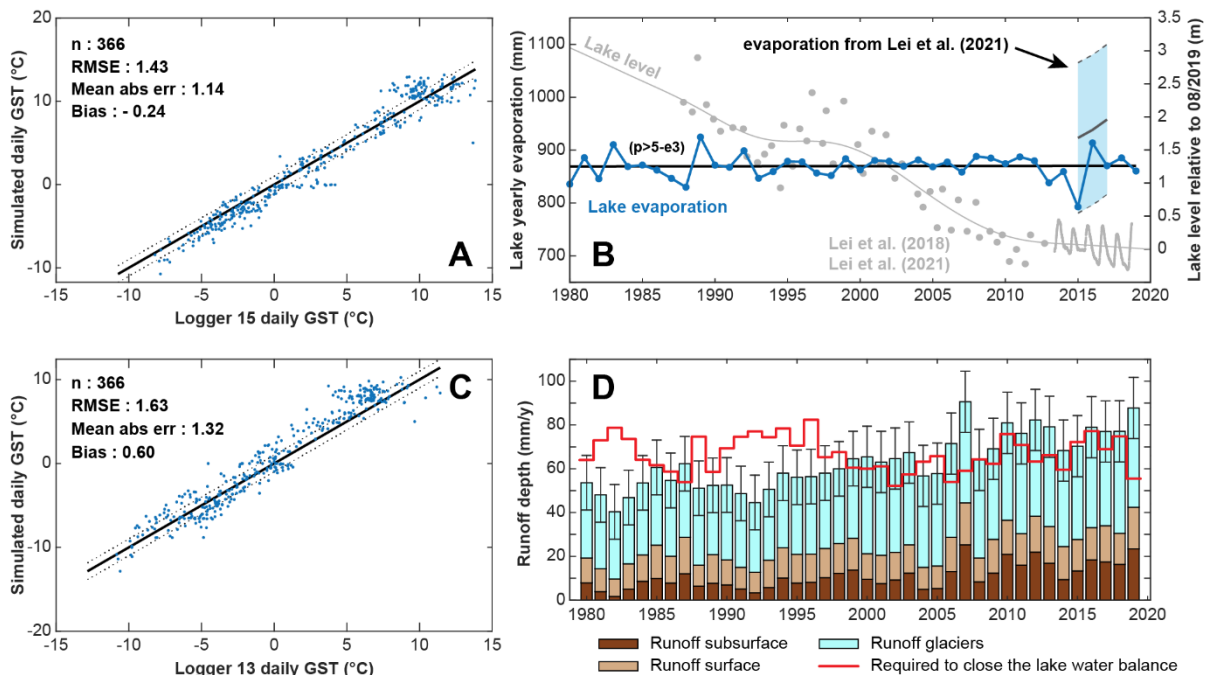
Figure 5. Model validation. A and C: modeled mean daily ground surface temperatures compared to measured ground surface temperatures for logger 15 and logger 13 (location on Fig. 1). B: modeled annual lake evaporation (blue curve) and comparison with values calculated by Lei et al. (2021) in the light blue zone. The gray curve shows the smoothed lake level relative to August 2019 based on observations from Lei et al. (2018) (gray points) and Lei et al. (2021) (gray oscillating line). D: Comparison between the runoffs required to reproduce the observed lake variations (red curve, derived from lake level, lake area, forcing data and lake evaporation) and the sum of the glacier and land runoff we derive from remote sensing observations and modeling respectively (Sect. 3.2). Error bars are associated to the glacier values and come from the geodetic results. Runoff values are expressed as heights scaled to the land surface of the Paiku catchment.

Annual lake evaporation mainly ranges between 800 and 900 mm per year (Fig. 5B), with a mean value of 870 ± 23 mm (1σ). Lake evaporation does not exhibit a linear trend of increase or decrease and is mostly dominated by year-to-year variability. Though slightly lower, our evaporation results are in

389   good agreement with the values from Lei et al. (2021), which are derived from local and regional

390   meteorological observation and lake budget calculation (Fig. 5B). We used the simulated evaporation

391   together with the lake level data and lake area data from Lei et al. (2018) and Lei et al. (2021) and the

392   precipitation forcing datasets (3.2.2) to derive the total runoff (land + glacier) required as an input to

393   the lake budget to reproduce the lake variations. This required runoff corresponds to the red line of

394   Fig. 5D. The required runoff volumes are scaled to the land area of the catchment to be comparable

395   with the other variables. Fig. 5D also presents the runoff values derived from the land cryo-hydrological

396   modeling and from the glacier remote sensing investigations. Annual volumes are expressed as mm

397   over the land part of the catchment (excluding the lake). As presented in section 3.2.6, glacier mass

398   balance values are considered constant for the 1980-2000 period and the 2000-2019 period and are

399   respectively equal to -4.6 ± 2.5 10^7 and -6.4 ± 2.8 10^7 m³ per year. The addition of annual precipitation

400   to these values to quantify the total glacier runoff introduces year-to-year variability to the glacier

401   runoff. At the catchment scale, the average glacier runoff over the 40 years is 39 ± 13 mm per year.

402   Over the 40 years, the average annual land runoff value (surface + subsurface) we model is 24 ± 8

403   mm. Summed together, the land and glacier runoff find a partial agreement with the runoff that is

404   required to close the lake water balance. Annual values are compatible within error bars for 28 out of

405   the 40 years of simulations. The glacier and land runoff are slightly too small to close the lake water

406   balance during the first 20 years and slightly too large for the last 20 years of simulation. Over the whole

407   period, the sum of the glaciers + land runoff produces 95% of the required runoff. Land runoff is further

408   described in Sect. 4.3 and lake results in section 4.4.

409   *4.1.2. Hydrological budget of Lake Paiku*

410   Our observations, climate data, simulations, geodetic data and the lake level data from Lei et al.

411   (2018, 2021) enable us to quantify the different terms of the lake hydrological budget. We present these

412   results in m of lake level change based on the average slope of the Volume = f(level) relationship

413   (Fig. 6). As the unique output term, evaporation dominates the lake budget with an average annual value

414   of 0.86 m (34.6 m per 40 years, Fig. 6A). Direct precipitation in the lake is the dominant input with an

415   average annual value of 0.31 m (12.3 m per 40 years), followed by glacier runoff (0.28 m per year, 11.3

416 m per 40 years) and land runoff (0.18 m per year, 7.0 m per 40 years). When compared with lake volume

417 observations over the 40 years of the simulation, the simulated lake budget is 1.04 m too negative.
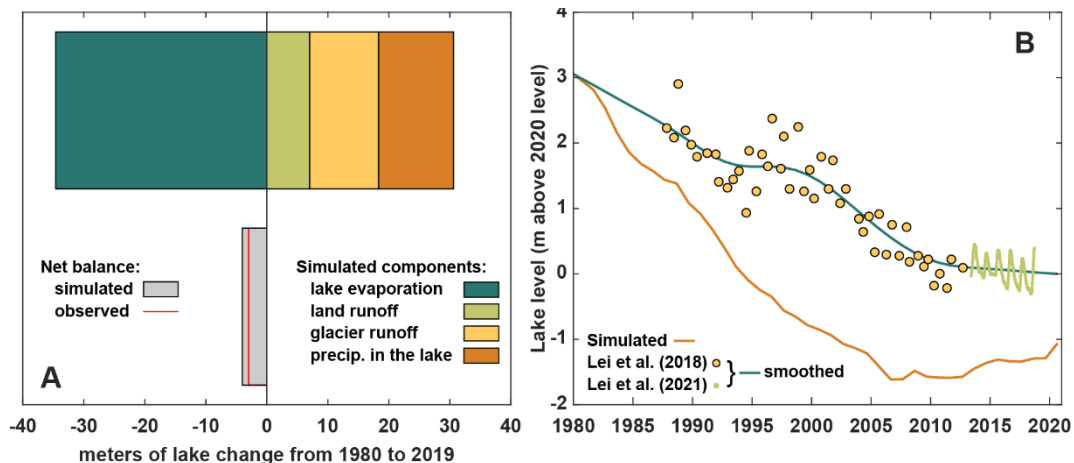
418
419 *Figure 6. Budget and level of lake Paiku for the simulation period (1980-2019). A. The different*
420 *components of the hydrological budget of the lake according to our framework. Results are given in m*
421 *of lake change based on the average slope of the Volume = f(level) relationship. B. Lake level data.*
422 *Points correspond to observations from Lei et al. (2018, 2021) that we smoothed (green curve, based*
423 *also on observation points older than 1980). The simulated lake level appears in orange.*
424

425 Based on our results, we also reconstructed lake level variations that we compare with the observed

426 variations (Fig. 6B). Following our framework, our values are presented at an annual timestep. They

427 qualitatively reproduce the overall lake level decrease but tend to overestimate this decrease and show

428 an increasing mismatch with the observations from 0 in 1980 to 2 meters in 2005. This mismatch is

429 later compensated by an increasing lake level trend in our simulation from 2005 to 2019. At the end of

430 the simulation period, the mismatch is 1.04 m, consistent with the budget values (Fig. 6A) and the fact

431 that our approach provides 95% of the required runoff to close the lake budget (Sect. 4.1.1.). This pattern

432 of a too strong decrease followed by an increase is consistent with the comparison between simulated

433 and required runoff presented on Fig. 5D.

434 ## 4.2. Ground thermal results

435 Based on our temperature results, we define four categories of ground thermal regimes (Fig. 7A).

436 *Cold permafrost* are the areas of the catchment for which the deepest thaw depth did not exceed 1 m

437 over the 40 years of simulation. For cold permafrost, frozen conditions dominate the first meters of the

438 ground most of the year and surficial thawing during summer can be interrupted by ground freezing

from the surface to the top of the permafrost at night. *Warm permafrost* are the areas of the catchment

presenting permafrost for the whole duration of the simulation and which are not part of the *cold*

permafrost. These areas are characterized by a distinct seasonal pattern of frozen ground in winter and

an active layer in summer. *Disappearing permafrost* are the areas of the catchment presenting

permafrost at the beginning of the simulation and not at the end. *No permafrost* are the areas without

permafrost at the onset of the simulation. The geographical characteristics of each ground category are

presented in Tab. 1, and their distribution throughout the catchment is shown on Fig. 7A. These different

ground categories are subsequently used to compare their cryo-hydrological behaviors during the

simulation (consistent color code).

Table 1. Cryological classification of the catchment based on the modeled ground temperatures.

Name	Characteristics	% of the catchment area	Elevation mean (masl)	Elevation range (masl)	Slope mean (°)
Cold permafrost	Max thaw depth over the 40 years < 1m	3%	6068	6946 5213	35±13
Warm Permafrost	Max thaw depth > 1 m and permafrost present over the 40 years	19%	5480	5921 4877	20±9
Disappearing permafrost	Permafrost present in 1980 but disappears during the simulation	5%	5274	5552 4882	18±9
No permafrost	No permafrost from 1980 to 2019	73%	4900	5463 4580	10±8

At the catchment scale, the 2 m depth temperature (Fig. 7B) shows a pronounced warming trend

of 0.17 °C per decade ($p=1\times10^{-6}$). This trend is mainly supported by the *no permafrost* areas, which

underwent a slightly stronger warming trend of 0.2 °C per decade ($p=7\times10^{-8}$). Areas with disappearing

permafrost, warm permafrost and cold permafrost exhibit smaller trends around 0.1 °C per decade with

decreasing p-values (respectively 0.00001, 0.006 and 0.05, i.e. non-significant for the last two).

From 1980 to 1989, permafrost covers 27% of the catchment and the mean active layer thickness

(ALT) is 1.36 ± 0.51 m (1σ, minimum: 0.11 m and maximum: 2.37 m, Fig. 7C). From 2010 to 2019,

permafrost covers 22% of the catchment. At the scale of the initial permafrost area, this change

corresponds to a loss of 19%. The mean ALT is 1.29 ± 0.49 m (1σ, minimum: 0.11 m and maximum:

2.55 m, Fig. 7D) for this period. Permafrost disappearance (grey zones in Fig. 7D) mainly happens for

459   low-lying permafrost of the south and the center of the catchment. It occurs for the most part on the

460   outer slopes of the permafrost regions and at the bottom of steep glacial valleys.
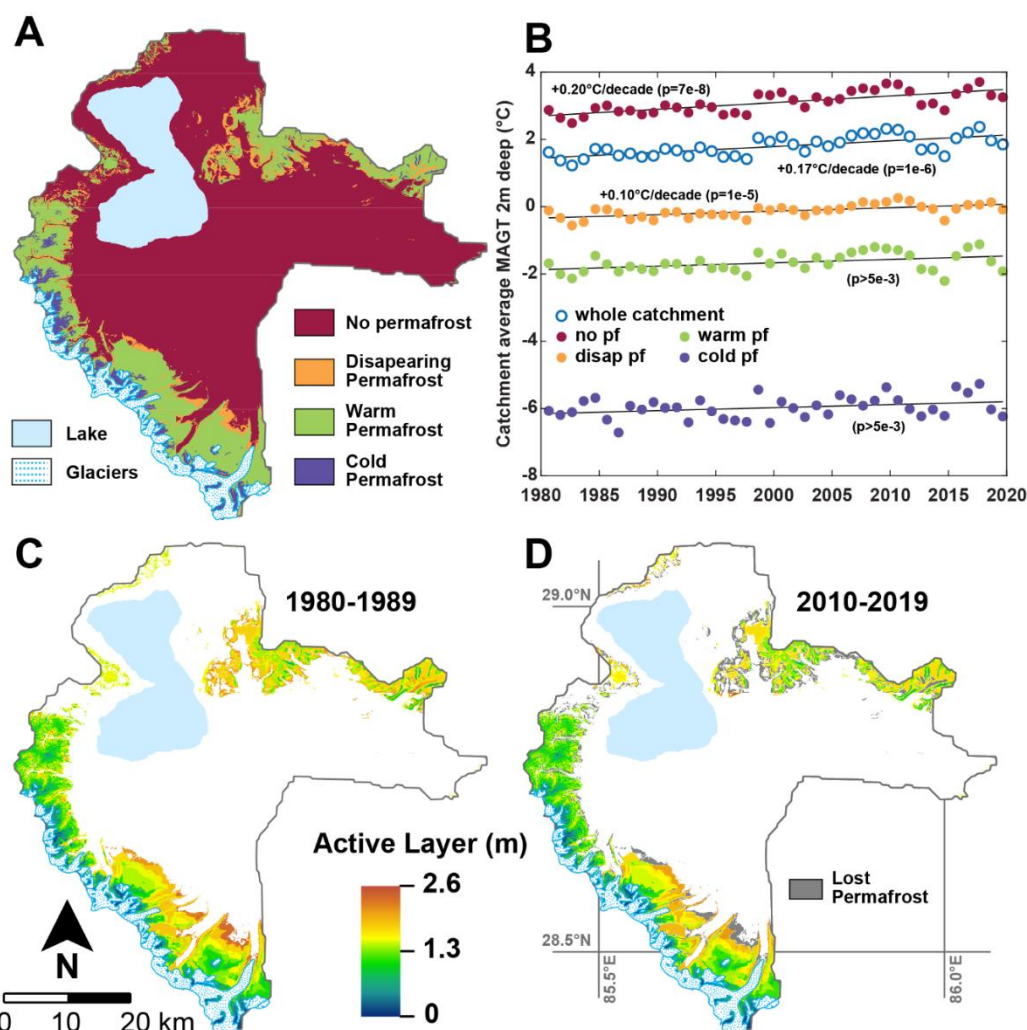
461
462 *Figure 7. A: Different cryological states of the ground throughout the catchment for the 1980-2019*
463 *period (see Tab. 1). B: Annual 2 m deep ground temperature averaged for the whole catchment and for*
464 *the different cryological states of the ground. C: Average active layer depth over the 1980-1989 period.*
465 *D: Average active layer depth over the 2010-2019 period. Only locations presenting permafrost at the*
466 *end of the simulation are assigned a color on the map on C and D. Locations where permafrost has*
467 *disappeared are shown in gray on D.*
468
469   We also present the average duration of seasonal thaw at a depth of 70 cm averaged over the

470   catchment (Fig. 8A). Because at this depth some areas might present two (or more) consecutive years

471   without thawing (highest locations) or without freezing (lowest locations), these areas were excluded

472   from the averaging. In the end, the averaged results account for 89% of the catchment land area (i.e.

473   excluding glaciers and lake Paiku). The results show an increasing trend in the duration of the seasonal

474   thaw of +4.6 days per decade (p=3×10⁻⁴, blue line on Fig. 8A). When looking at the average start and

475   stop days of the seasonal thaw (Fig. 8A, grey lines) in the Julian calendar (day 150 is the 30th of May

476 and day 300 is the 27th of October), we note that this increase is mainly caused by a later ending date of

477 the thaw season (*Stop date* on Fig. 8A, +6.1 days per decade, p=8×10⁻¹⁰) and not by an earlier starting

478 date (non-significant trend).
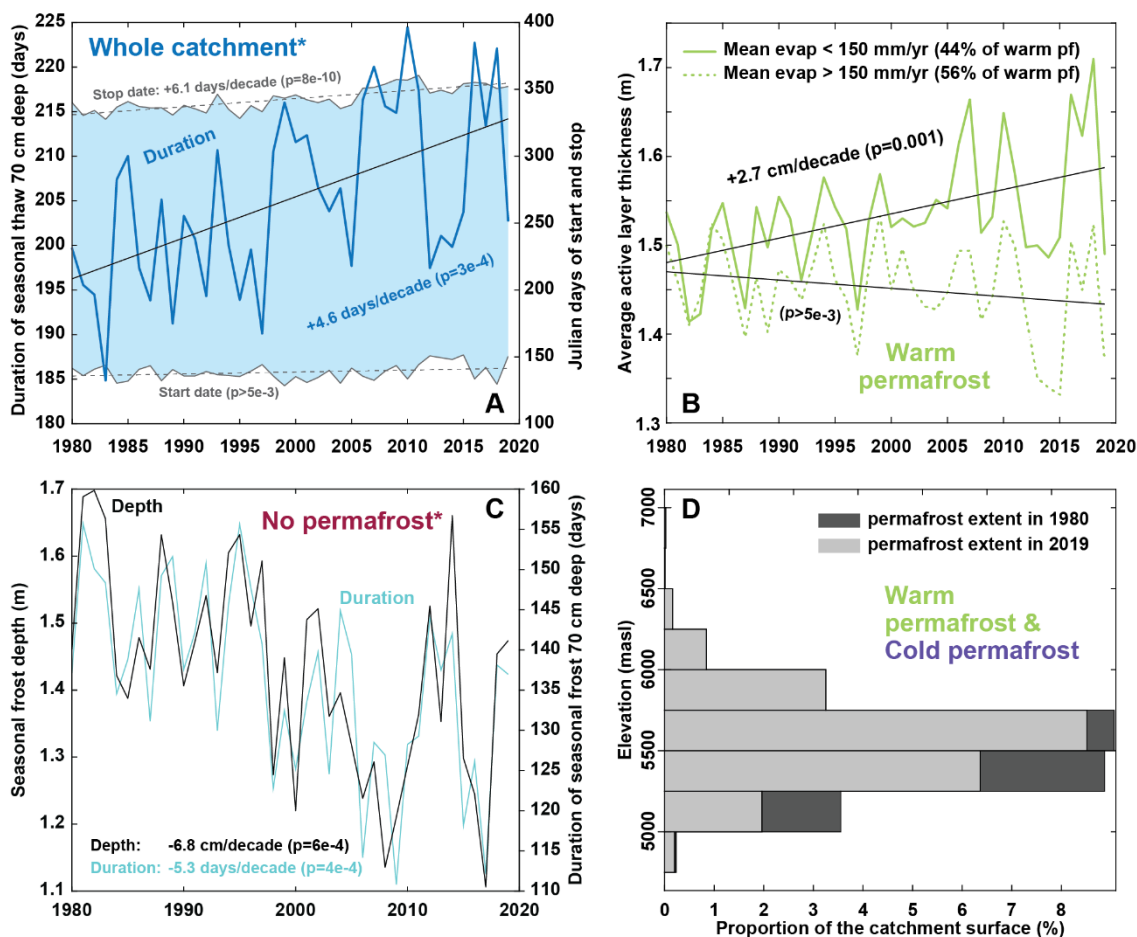
479
480 *Figure 8. A: Duration of seasonal thaw 70 cm deep averaged over the catchment. The asterisk indicates*
481 *that the presented curves average 89% of the surface of the catchment (Sect. 4.2). The gray curves and*
482 *the light blue area are associated with the right axis and indicate the average start and stop day of the*
483 *seasonal thaw in the Julian calendar. Values higher than 365 indicate that freezing conditions came*
484 *back after the 31st of December. B: Active Layer Thickness (ALT) evolution for warm permafrost. The*
485 *solid line shows the ALT for simulations experiencing an annual evaporation lower than 150 mm when*
486 *averaged over the 40 years. The dashed line shows the ALT for simulations with annual evaporation*
487 *higher than 150 mm. C: Temporal trends for seasonally frozen ground where there is no permafrost.*
488 *The asterisk indicates that simulations were excluded if one of the simulated years did not present*
489 *freezing conditions 70 cm deep (persistence of thawed conditions from one year to another). The*
490 *presented curves thus average 88% of the total permafrost-free areas of the catchment. D: Altitudinal*
491 *distribution of permafrost in 1980 and 2019. This distribution includes both cold and warm permafrost.*
492
493   Within *warm permafrost*, we distinguished ALT for locations experiencing an average evaporation

494 lower or higher than 150 mm per year during the simulations (Fig. 8B). Whereas locations with average

495 evaporation below 150 mm per year record an active layer deepening trend of 2.7 cm per decade

(p=0.001), it is not the case for locations with an average evaporation higher than 150 mm per year (non-significative trend).

In the permafrost-free areas of the catchment, seasonal frozen ground (Fig. 8C) reaches a depth of 1.43 ± 0.15 m on average and shows a decreasing trend of -6.8 cm per decade (p=6×10^{-4}). At a 70 cm depth, the average duration of seasonally frozen ground is 136 ± 12 days with a decreasing trend of -5.3 days per decade (p=4×10^{-4}). These values average 88% of the no permafrost areas since locations showing persistent thawed conditions at this depth from one year to another were excluded (i.e. minimal seasonal freezing depth over the 40 years lower than 70 cm).

When comparing permafrost spatial distribution between 1980 and 2019 (Fig. 8D), our results show that permafrost distribution above 5750 masl has not been modified during the simulation. Permafrost disappearance has mainly occurred between 5000 and 5750 masl, with the largest loss reaching 2.5% of the catchment area between 5250 and 5500 masl.

4.3.   Hydrological results for the land

The mean annual evaporation (land area only) over the simulation time is 180 ± 19 mm (1σ, Fig. 9A). Evaporation shows an increasing trend over the 40 years of +1.01 mm per decade (p=3×10^{-7}). Average total runoff over the 40 years is 24 ± 8 mm per year (Fig. 9B) and exhibits an increasing trend of +4.8 mm per decade (p=8×10^{-7}). Similarly, surface runoff (13 ± 3 mm per year) and subsurface runoff (11 ± 6 mm per year) show increasing trends of +1.3 and +3.5 mm per decade (p=6×10^{-5} and 3×10^{-7}) respectively (Fig. 9B). The surface runoff presented on Fig. 9B includes the snow melt that did not infiltrate the ground. These linear trends we report are high compared to the absolute values of the variables and their extrapolation backward in time would lead to null values in the recent past which is unrealistic. This suggests a non-linear evolution of these variables over the XXth century.

We also present the catchment average of the *runoff / (runoff + evaporation)* ratio (Fig. 9C), which is equivalent to *runoff / (rain + snow – snow sublimation)* given the negligible contribution of soil storage variations. Hence it is the proportion of the water input to the ground surface that is converted

521   into runoff. This proportion is $11 \pm 2\%$ over the simulation time and shows an increasing trend of

522   +1.23% per decade ($p=2\times10^{-7}$). Fig. 9C also shows the average theoretical ratio to maintain a steady

523   lake level (of 17.6%). This ratio was obtained under the following hypothesis:

524   •   Same climate forcing data, hence same lake evaporation

525   •   The glacier contribution is (i) considered the same for the historical simulation and this

526   scenario and (ii) taken as the difference between the total land surface runoff and the red

527   curve of *required runoff* in figure 5, therefore independent of remotely sensed estimates.

528   •   Under these conditions, the runoff increase needed to maintain the lake level is only

529   supplied by land runoff (surface and subsurface) by shifting the *runoff / (runoff +*

530   *evaporation)* ratio.

531   The ratio from the historical simulation starts significantly below the theoretical steady lake ratio

532   (10.2% < 17.6%, Fig. 9C) and increases progressively to 16.0% in 2019.

533   Finally, Fig. 9D shows the annual proportion of *liquid / total* water averaged for the whole

534   catchment. The value was computed based on the daily water content (liquid and frozen) of the first

535   2 m of the soil column (the hydrologically active part of the column, Sect. 3.2.4) from which annual

536   averages were derived and used to compute a catchment scale average. The graph indicates that the

537   proportion of liquid water in the total water content increases at around +1.41% per decade ($p=1\times10^{-4}$),

538   indicating an increasing availability of liquid water in the ground with time.
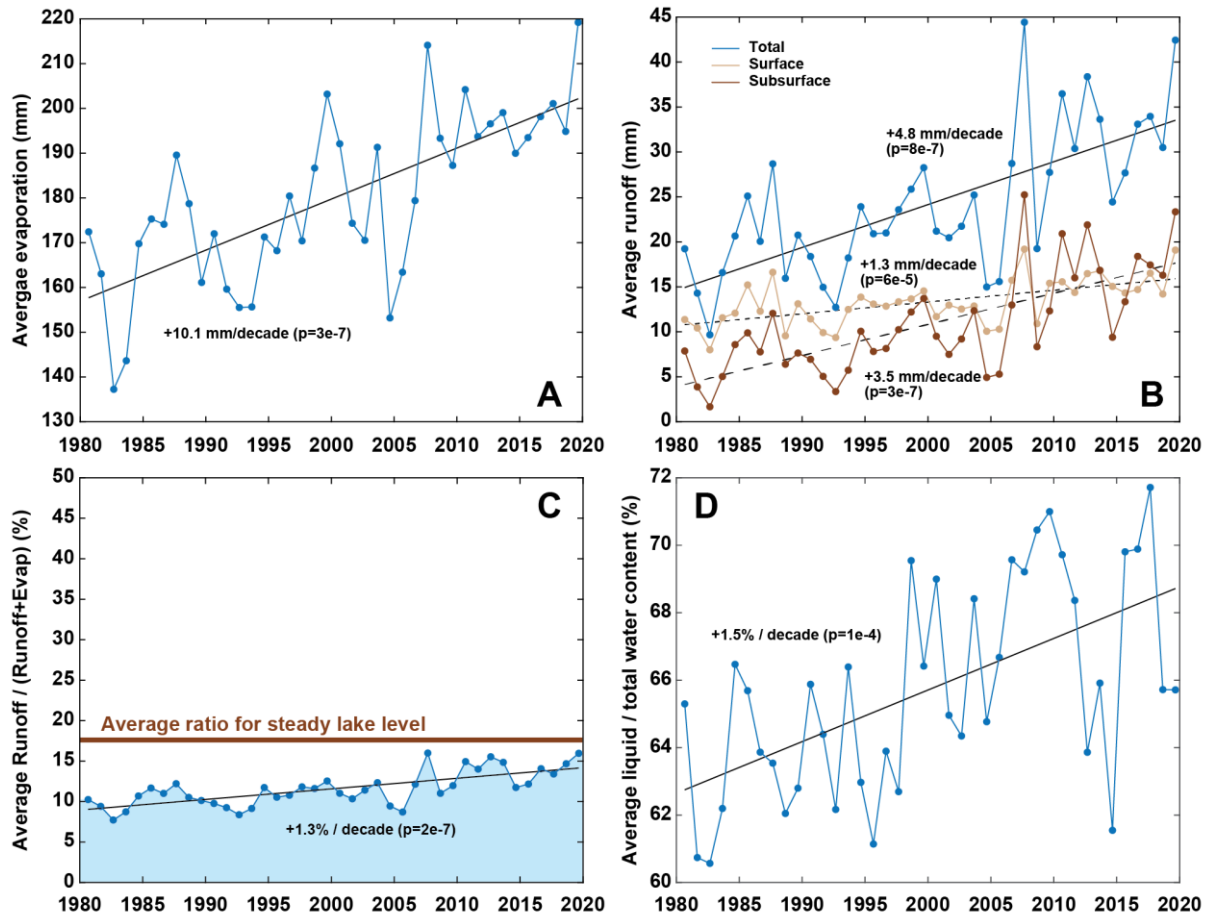
Figure 9. Hydrological results. *A*: *Annual* evaporation *averaged over the whole catchment. B: Annual runoff averaged over the whole catchment. The blue curve sums the surface and subsurface runoff. C: Ratio between runoff and (evaporation + runoff) averaged over the whole catchment. The brown line indicates the theoretical average ratio needed to maintain a steady lake level when considering an identical glacier contribution to runoff (details in Sect. 4.3). D: Annual mean of the (liquid water)/(total water) ratio over the first 2 meters of ground, averaged over the whole catchment.*

4.4. Sensitivity test on evaporation and runoff

We conducted a simple sensitivity test on the climatic conditions. We ran the same 40 years of simulations (with thermal initialization) for a climate 1 °C cooler and 30% wetter (more precipitation) than the historical scenario. We call this new scenario *colder and wetter* (to be compared with the *historical scenario*, i.e. the results of the present study presented in the rest of Sect. 4). Results of this experiment are presented in Fig. 10 and Table 2. Because of the difference in climate forcing, the *colder and wetter* scenario produced a greater amount of *cold* and *warm permafrost* areas than the historical scenario, as presented on Fig. 10A. Fig. 10B shows the proportion of the precipitation reaching the

555   surface (rain + snow – snow sublimation) that produces runoff compared to evaporation for the Paiku

556   catchment. Figure 10C aggregates over the whole catchment the distribution of such precipitation input

557   to the ground between runoff and evaporation for both scenarios. In between them, it also includes the

558   distribution associated with the steady lake level scenario of Fig. 9C, which is based on the hypothesis

559   listed as bullet points in Sect. 4.3 (climate forcing of the historical scenario, same glacier contribution,

560   only land runoff increases).
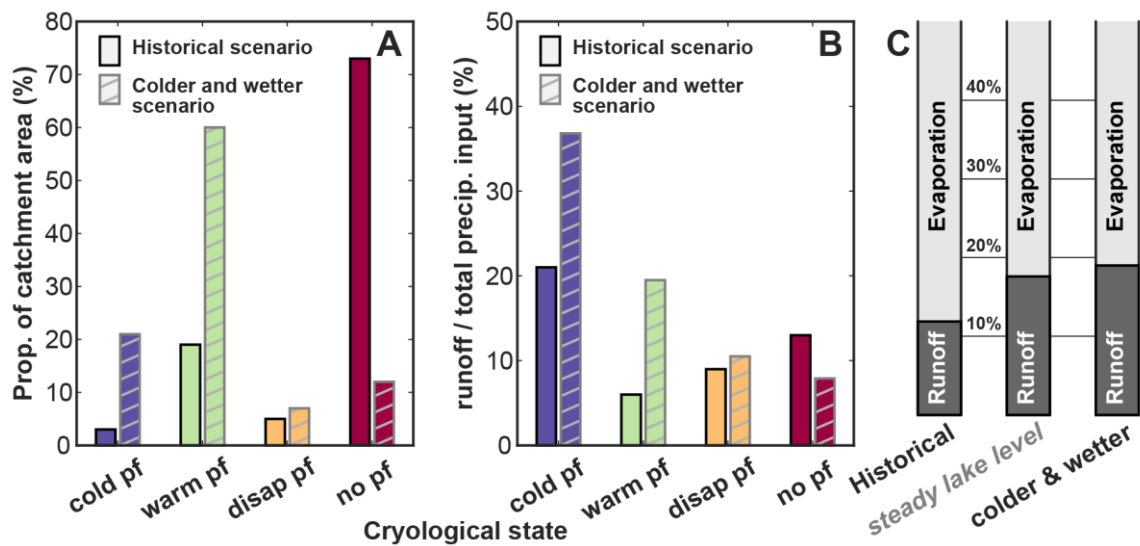
561
562   *Figure 10. Sensitivity of the distribution between runoff and evaporation to climate. A: distribution of*
563   *the different cryological states of the ground for the historical scenario (presented in Section 4) and for*
564   *an alternative scenario where the climate is 1 °C colder and brings 30% more precipitation. B: runoff*
565   *as a proportion of the precipitation input to the land (rainfall + snowfall – snow sublimation) for the*
566   *different cryological states of the ground and for the 2 climatic scenarios. C: catchment scale ratio*
567   *between runoff and evaporation for (i) the historical scenario, (ii) for a steady lake level with the same*
568   *glacier contribution (same as Fig. 9C), and (iii) for the colder and wetter scenario.*
569
570   The *historical scenario* shows that *cold permafrost* areas produce the highest proportion of runoff,

571   which we attribute to the fact that the ground in these areas is most of the time frozen, turning a

572   substantial part of the snow melt and rainfall into surface runoff. When considering grounds with a

573   hydrologically active subsurface (*warm permafrost*, *disappearing permafrost* and *no permafrost*) in the

574   historical scenario, the proportion of runoff increases slightly from *warm permafrost* to *no permafrost*.

575   Such an evolution then corroborates the idea that the presence of permafrost tends to increase

576   evaporation at the expense of runoff, as modeled by Sjöberg et al. (2021). Yet, for the *colder and wetter*

577   scenario, runoff shows a regular decrease from *cold* to *no permafrost* with a more pronounced trend

578   than the historical scenario. Several factors can be at play in this transition and most likely involve (i)

579 a different extent and altitudinal distribution for each cryological type of ground, (ii) an overall reduced

580 intensity of evaporation due to cooler surface temperatures, (iii) a higher soil water content driven by

581 higher precipitation and (iv) difference in the seasonal timings. Altogether, these processes substantially

582 change the proportion of water that ends up as runoff water available for the lake, as highlighted by Fig.

583 10C.

584 *Table 2. Distribution of between runoff and evaporation for the 2 scenarios*

Ground cryological type	**Historical Scenario**			**Colder and wetter scenario**		
	Precipitation input[1]	Runoff	Evaporation	Precipitation input[1]	Runoff	Evaporation
Cold permafrost	*100%* 117 mm	*21%* 24 mm	*79%* 93 mm	100% 234 mm	37% 86 mm	63% 148 mm
Warm permafrost	*100%* 183 mm	*6%* 10 mm	*94%* 173 mm	*100%* 281 mm	*20%* 55 mm	*80%* 226 mm
Disappearing permafrost	*100%* 211 mm	*9%* 19 mm	*91%* 192 mm	*100%* 211 mm	*10%* 22 mm	*90%* 189 mm
No permafrost	*100%* 218 mm	*13%* 28 mm	*87%* 189 m	*100%* 200 mm	*8%* 16 mm	*92%* 184 mm

585 *[1]. Precipitation input is the input to the ground, counted as rainfall + snowfall – snow sublimation*

5. Discussion

5.1. Limitation and potential of the approach

5.1.1. Data usage within the conceptual framework and data scarcity

Our approach relies on a variety of data regarding their scientific focus (glaciers, ground, lake, atmosphere), their type (in situ observations, remotely sensed data, reanalysis data), their characteristics (point wise data, distributed data, constant or with various time resolution) and the way they interact with our models (model parameters, forcing data, validation data, result data in case of the glacier runoff). Such a diversity arises from our goal to quantify both the ground thermo-hydrological regime and the different terms of the lake budget. This variety also makes it challenging to consistently merge these data into a unique framework. For example, our quantification of the glacier mass change reconstruction is made of two constant values for the study period (1975-2000 and 2000-2020), which limits the relevance of the comparison between the observed lake level variations and the simulated ones.

Yet, the lake level variations are the only hydrological observations available to evaluate the robustness of the runoff we compute. Therefore, we had to combine lake level observations with our precipitation forcing data and lake evaporation quantifications in a simple mass conservation calculation, to derive the land runoff to the lake required to reproduce the level variations (red curve on Fig. 5D). In this regard, the sum of the glacier and land runoff we derive over the 40 years correspond to 95% of the required runoff to the lake, indicating that the magnitude of our reconstruction is correct. Year-to-year comparison is less accurate and we suggest that this is the consequence of the aforementioned limitations and also of our modeling strategy as detailed below.

A main limitation regarding our usage of the data is related to the limited amount of available field observations required to provide robust model parameterizing, climate forcing and in-depth validation of the simulations, both hydrologically and thermally. Regarding climatic forcing data, our AWS measurement offers sound observations to evaluate and adjust the ERA5 data processed with TopoSUB and downscaled with TopoSCALE. Yet, a period of observations longer than 2 years would have enabled more robust corrections and could have allowed us to perform a more advanced statistical

613 downscaling approach, e.g. quantile mapping (Themeßl et al., 2011). As such, the spatiotemporal

614 domain of relevance of these corrections is insufficient to correct data for the whole catchment and the

615 40 years of simulations. Overall, considering the strong bias we observe in the raw ERA5 data (Figure

616 D1), these corrections do represent an important first-order improvement. Altogether, this scarcity of

617 field observations is likely to bring significant uncertainties to our analysis. Future efforts should focus

618 on acquiring additional data or developing validation methods based on remotely sensed observations.

619 ### 5.1.2. Modeling strategy

620 By giving access to the timing of water transport across the catchment, water routing would allow

621 to investigate temporal hydrological patterns at a monthly or seasonal scale. Because we work at annual

622 and decadal time scales, this limitation has limited consequences on our results. The main consequence

623 is to ignore potential storage effects on the land that would delay the arrival of runoff to the lake. We

624 suggest that this limitation contributes to explaining the limited match between computed and required

625 runoff at the annual time scale (Fig. 5). Yet, our subdivision of the catchment based on the different

626 cryological states of the ground allows us to work with hydrological units that are smaller than the

627 catchment and thus present shorter hydrological response time to precipitation.

628 Additionally, our approach regarding the modeling of runoff is relatively simple, i.e. partition

629 between subsurface and surface runoff based on comparison between the soil water content and field

630 capacity and porosity, respectively. More complex approaches split runoff into more sophisticated

631 categories such as Horton overland flow, Dunne overland flow, subsurface stormflow… (e.g. Savenije,

632 2010; Gao et al., 2014; Mirus and Loague, 2013). However, over the last decade, the relevance of this

633 type of partitioning between different types of runoff has been questioned (McDonnell, 2013; Gao et

634 al., n.d.). In the frame of our study, we find it important to distinguish between surface and subsurface

635 runoff because they generate flows with very contrasted speed. In a general perspective, this significant

636 difference in flow velocities impacts the hydrological system as a whole (e.g. river discharge,

637 evaporation…) and has various consequences throughout the catchment, such as the water availability

638 for vegetation, erosion and sediment transport.

639   In the particular case of a cryo-hydrological study, separating surface from subsurface runoff is

640   particularly relevant because both flows do not react in the same way to ground temperature changes.

641   As such, we see our approach as a middle way that allows us to make this distinction based on simple

642   hydrological considerations. Yet, we acknowledge that the classification and quantification of the

643   different types of runoff represent a valuable direction for future investigation on catchment-scale cryo-

644   hydrology in Tibet. Another potential improvement in our modeling approach could be to unravel

645   evaporation from transpiration. However, since vegetation is extremely scarce in the Paiku catchment,

646   which is largely dominated by barren lands, we suggest that this would not significantly affect our

647   results. However, this limitation should be explored in future field and modeling studies.

648   Conversely, our approach also conveys several important advantages regarding our goal to

649   describe and quantify the ground thermo-hydrological regime of the catchment. The use of TopoSUB

650   enables us to produce results at a resolution of 100 x 100 m over an area of nearly 2400 km^2 with

651   calculation costs 700 times lower than if each 100 x 100 m pixel was treated individually. Yet, thanks

652   to the clustering method used to produce the forcing dataset (Sect. 3.2.2), the strong spatial variability

653   of the physiography and its impact on the climate and incoming radiations is significant in the forcing

654   data and has a major influence on the ground thermo-hydrological results, as exemplified by the strong

655   spatial variability of ground temperatures (Fig. 7). Beyond elevation, other physiographic parameters

656   such as aspect also influence the results. The mean values of 2 m-deep temperature and evaporation

657   over the 40 years for north-facing areas (averaged over the whole catchment and over the 40 years) are

658   1.3 °C and 163 mm while they reach 2.9 °C and 197 mm for the south-facing ones. This strong

659   dependence of modeled results on physiography highlights the necessity to take it into account when

660   modeling the thermo-hydrological regime of the ground in high mountainous environments. Finally,

661   our approach allows us to couple the physical processes governing both energy and water fluxes at the

662   surface and subsurface and highlight their interplay, as developed in section 5.1.4.

663   *5.1.3. Reconstruction of the Lake hydrological budget and level variations*

664   The total lake level change we simulate is a decrease of 4.11 m. This is qualitatively consistent

665   with the overall observed trend. The mismatch with the observations is limited to a 1.06 m excess in

666   the simulated level drop (Fig. 9A). Our reconstruction shows a decrease of 4.66 m from 1980 to 2007,

667   which is an overestimation of the initial drop. Afterwards, while observations indicate a gradual

668   slowdown of the lake level decrease, we simulate a stabilization followed by a slight increase (0.55 up

669   between 2013 and 2019).

670   A possible reason for this mismatch is that the lake is connected to a larger aquifer that surrounds

671   it. In the context of a decreasing lake level, an aquifer surrounding the lake can create an additional

672   water inflow when the lake level passes below the piezometric level of the aquifer (Yechieli et al.,

673   1995). Such an inflow could mitigate the lake level decrease and thus explain the missing water in our

674   reconstruction (Fig. 6B). It could also explain the gradual stabilization of the lake level that our model

675   does not reproduce. This flow is not part of our conceptual hydrological framework even though it likely

676   exists in reality, especially since there is no permafrost near the lake (as we simulate it here), allowing

677   for the existence of such an aquifer (Walvoord and Kurylyk, 2016). Groundwater has been identified as

678   a potential contributor to lake level rise in other regions of the QTP (Lei et al., 2022). In the long run,

679   lake-aquifer systems commonly follow oscillations of the net atmospheric flux of water (Precipitation

680   – Evaporation) and of the runoff that forces its mass balance (Watras et al., 2014). During these

681   oscillations, the lake can "pump" water from the aquifer or feed it depending on the relative difference

682   of piezometric level between them (Almendinger, 1990; Liefert et al., 2018). Yet, this potential effect

683   is difficult to account for and its magnitude remains unclear. Therefore, the reasons for the mismatch

684   between observed and simulated lake levels could also be connected to other aspects of our

685   methodology such as bias in the climatic forcing data and other shortcomings arising from the lack of

686   field data, or hydrological processes, as developed in Sect. 5.1.1 and 5.1.2.

687   Our reconstruction of the lake budget is informative regarding the respective contribution of the

688   different inputs and outputs. Regarding lake evaporation, our mean value of 870 ± 23 mm is close to

689   the one modelled by Yang et al. (2016) with the Flake model for lake Nam (832 ± 69mm) for the period

690   1980-2014 but we do not report a significant increasing trend in our results. Yet for the same lake (Nam

691   Co) and a similar period (1980-2016) Zhong et al., (2020) reported an average value of 1149 ± 71 mm

692   (along with an increasing temporal trend) using the Penman formula (Penman, 1948), thus highlighting

693   the potential dependence of the results to the methodology. In our results, direct precipitation to the lake

694 represents 40% of the inputs, followed by glacial runoff (35%) and land runoff (25%). Glaciers are

695 therefore a particularly important contributor to the runoff towards the lake (60% of the total runoff, vs.

696 40% for land runoff), what contrasts with the results from Biskop et al. (2016) who calculated that the

697 runoff input to the lake Paiku was dominated by land runoff (70% vs. 30% for the glacier contribution).

698 Here again, these difference likely arises from important differences in input data and methodologies

699 to quantify the different hydrological processes (evaporation, runoff, snow and glacier melt). Yao et al.

700 (2018) reported that, at the QTP scale, the balance between precipitation and evaporation (over land

701 and lake) was dominant over glacier melt to understand both lake storage increases and decreases. Our

702 reconstruction does not give us access to significant temporal variation of the glacier contribution but

703 the above-mentioned proportions in the contributions to the lake (40%, 35% and 25%) show that the

704 glacier contribution does not dominate the input terms. At the catchment scale, these proportions can

705 vary significantly depending on the glacier coverage. For Lake Selin, Zhou et al. (2015) reported that

706 runoff towards the lake, evaporation from the lake and on-lake precipitation altogether explained 90%

707 of the lake storage variations for the 2003-2012 period. The catchment of lake Selin has a very limited

708 glacier coverage, corresponding to 0,63% of its area (Lei et al., 2013), compared to the Paiku (5%).

5.1.4. The interdependence of thermal and hydrological variables

710 Our simulation results enable us to explore the interplay between the fluxes of energy and water at

711 the surface and subsurface. In this regard, we tested the correlation of evaporation with the proportion

712 of liquid/total water in the ground for cold and warm permafrost, as well as the correlation between

713 evaporation and the duration of seasonal thaw at a 70 cm depth (Fig. 11, A and B). For permafrost areas

714 (*cold permafrost* and *warm permafrost*), evaporation shows a strong correlation with the seasonal

715 distribution between liquid and frozen water, similar to previous modeling works for the region (Cuo

716 et al., 2015). As such, this correlation suggests that the intensity of seasonal ground thaw plays a role

717 in enabling higher or lower evaporative fluxes. This is likely due to cold surface temperatures strongly

718 reducing water loss from the surface and because moisture delivery to the surface is inhibited when the

719 ground is frozen. We suggest that this dependence is particularly important in the Paiku Catchment

720 because evaporation is strong (88% of the precipitation input to the surface evaporates on average) and

721   because frozen water is the dominant form of water in the ground in permafrost areas (Fig. 11A, the

722   calculation includes the first 2 meters below the surface).

723   Similarly, evaporation in *no permafrost* areas shows a significant correlation with the duration of

724   the seasonal thaw (Fig. 11B). We suggest that this result arises from the fact that frozen ground limits

725   the evaporative fluxes and thus years during which the subsurface seasonal thaw is shorter are associated

726   with reduced evaporative fluxes. We also tested the relationship between the linear trend of active layer

727   deepening and the mean evaporation (over the 40 years of simulation) for *warm permafrost* areas (Fig.

728   11C). Thus, this graph does not present annual values and one point corresponds to one of the 92

729   TopoSUB points classified as *warm permafrost* (values averaging the 40 years). The graph highlights

730   that TopoSUB points showing an Active Layer (AL) deepening trend are associated with low

731   evaporation and precipitation. From there, TopoSUB points with stronger evaporation show no

732   deepening trend or even a shrinkage of the AL. This relationship is contradicted by the highest level of

733   evaporation (>240 mm per year) observed for *warm permafrost*, for which AL deepening is observed

734   again (dark blue points of the graph). These TopoSUB points with the highest levels of evaporation also

735   correspond to those receiving the largest amount of precipitation. Further discussion on active layer

736   trends is provided in the next section.

737   Runoff also shows a strong connection with the ground thermal regime (Fig. 11D). At the

738   beginning of the simulation, years with an average 2 m-deep temperature below 0 °C are associated

739   with limited subsurface runoff (< 5 mm per year). Over the years, as the ground warms up and

740   permafrost disappears, subsurface runoff increases and can reach 20 to 45 mm per year. This result is

741   consistent with increased subsurface connectivity expected when permafrost thaws (Kurylyk et al.,

742   2014; Gao et al., 2021) that has been both observed (Niu et al., 2016) and modeled (Lamontagne-Hallé

743   et al., 2018; Huang et al., 2020; Gao et al., 2018). We suggest that these substantial changes in

744   subsurface runoff, associated with changes in the ground temperature in Fig. 11D support the hypothesis

745   of a modification in the hydrological pathways as permafrost thaws.
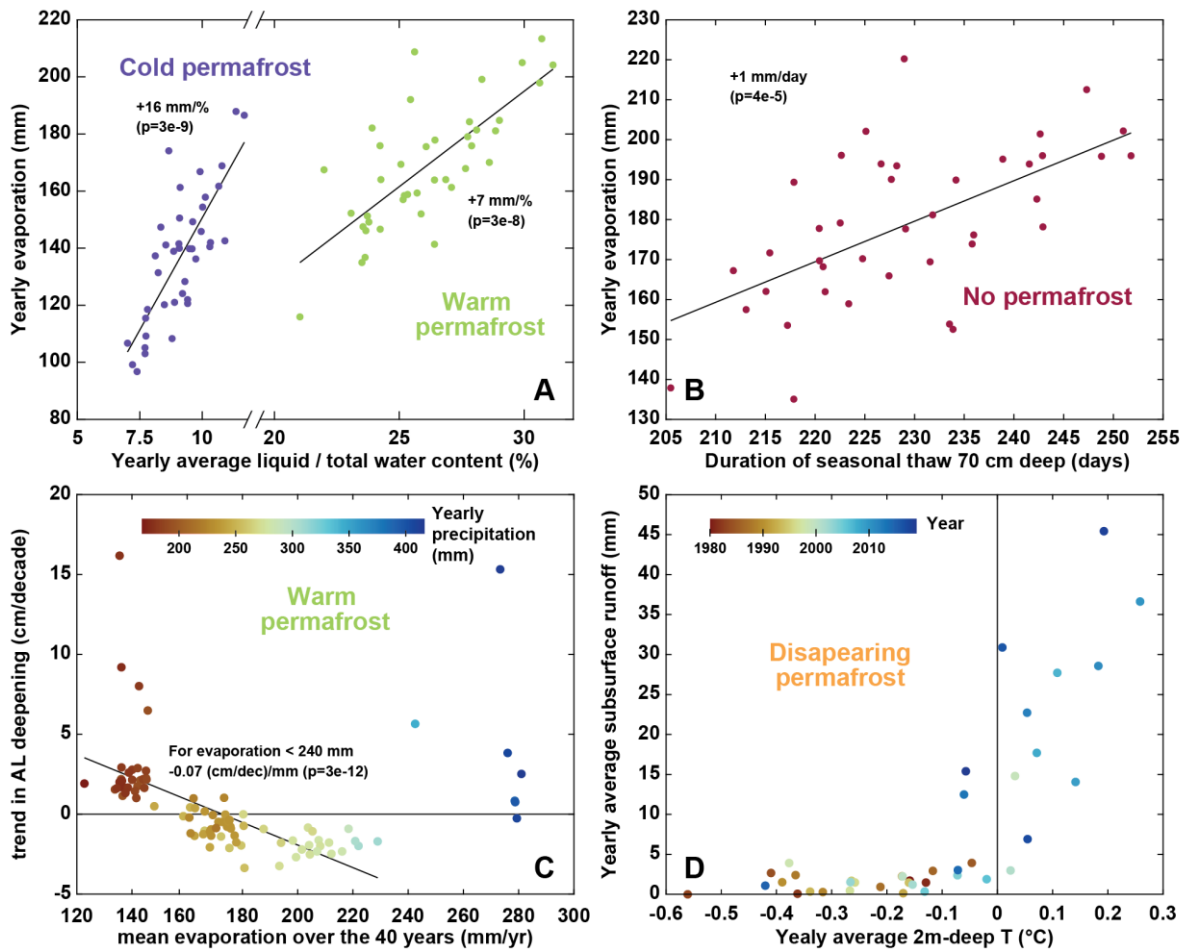
Figure 11. Thermo-hydrological couplings. A: Annual evaporation vs. annual mean of the liquid / total water ratio over the first 2 meters of ground, averaged for simulations corresponding to cold permafrost and warm permafrost (one dot per year for each permafrost category). B: Annual evaporation vs. duration of seasonal thaw at a 70 cm depth averaged for simulations corresponding to locations without permafrost (one dot per year). C: Active layer deepening trend vs. mean evaporation over the 40-year for each simulation corresponding to warm permafrost (here one dot corresponds to one TopoSUB point). The color of the dots shows the precipitations averaged over the 40 years for each simulation. The linear regression excludes simulations exhibiting annual evaporation higher than 240 mm. D: Annual subsurface runoff vs Annual 2 m-deep temperature averaged for simulations corresponding to locations with disappearing permafrost (one dot per year). The color of the dot indicates the year of the simulation.

Altogether, these results suggest a dependence of key variables quantifying the catchment hydrological balance (evaporation, runoff) to the seasonal characteristics and interannual trends of the ground thermal regime (temperature, liquid vs frozen water content). Similar to previous studies (Ding et al., 2020; Wang and Gao, 2022), we think these results advocate for the necessity to couple thermal and hydrological modeling to improve our ability to understand and quantify changes in the hydrological balance of high mountain catchments. To our best knowledge, along with Gao et al. (2022), our study represents to date the most complete effort to include the variety of coupled climatological,

surface and subsurface processes characterizing the climate, hydrology and ground thermal regime of high-mountain catchments in Tibet at a small scale with a high spatial resolution.

5.2. Cryo-hydrological trends in the catchment and across the QTP

5.2.1. Permafrost and ground temperature changes

Our results indicate that permafrost coverage in the Paiku catchment evolved from 27 to 22% of the land area during the simulated period. Such a coverage corresponds to sporadic permafrost (10-50% of the area) and is consistent with recent large-scale estimates of permafrost in the Northern Hemisphere (Obu et al., 2019) and across the QTP (Zou et al., 2017; Ran et al., 2018). This decrease corresponds to a 19% shrinkage of the 1980 permafrost area, which is higher than the 9% reported by Gao et al. (2018), a value determined by catchment-scale numerical modeling in the upper Heihe catchment (northeastern QTP) over a similar period. It is also slightly higher than the 13% decrease modeled from 1971 to 2015 for the Qinghai Lake catchment with a similar approach by Wang and Gao (2022). Yet, it is smaller than the 34% loss modeled by Qin et al. (2017) from 1981 to 2015 for the Yellow River Source Region (YRSR, North Eastern QTP).

Active layer (AL) evolution is contrasting throughout the catchment and a deepening signal is only visible for the locations with limited evaporation (<150 mm per year). Given the strong drive of summer climate on Active Layer Thickness (ALT), this overall lack of a deepening trend highlights how evaporation can act as an energy intake at the surface (Yang et al., 2014a), limiting the surface and subsurface heat fluxes and thus AL deepening. In this regard, our results fall in line with the conclusions of Fisher et al. (2016) when observing evapotranspiration and ALTs in boreal forests and also confirm the modeling experiments of Zhang et al. (2021b) on permafrost wetting in arid regions of the QTP. Besides, the lack of an overall deepening trend is consistent with observations from Luo et al. (2018) in the YRSR over the last decade and with the modeled AL from Zhang et al. (2019) at the scale of the QTP for the last 40 years. Where evaporation is limited, we report an AL deepening trend of 2.7 cm per decade, which is smaller than the 4.8 cm per decade trend modeled by Song et al. (2020) for the YRSR

791 for the same period, and smaller than the 4.3 cm modeled by Gao et al (2018) in the upper Heihe

792 catchment. Yet it is comparable to the 2 cm per decade value modeled by Wang and Gao (2022) for the

793 Qinghai Lake catchment from 1971 to 2015.

794   In *no permafrost* areas, our simulations show that the thickness of seasonally frozen ground shrinks

795 at a rate of 6.8 cm per decade. This rate is faster than the rate of 3.1 cm per decade quantified by Qin et

796 al. (2018) using the Stefan solution for the YRSR (1961-2016) and faster than the 3.2 cm per decade

797 modeled by Gao et al. (2018, Heihe catchment). However, it is similar to the 6 cm per decade rate

798 modeled by Wang and Gao (2022) in the Qinghai Lake catchment from 1971 to 2015 and smaller than

799 the 12 cm per decade modeled by Qin et al. (2017) for the YRSR (1981-2015). All these values fall

800 within the wide range of 3 to 29 cm per decade reported by Wang et al. (2020a) when studying

801 seasonally frozen ground over the whole QTP with in-situ observations. Regarding timing, we report a

802 decreasing trend of 5.3 days of frozen conditions (70 cm deep) per decade which is consistent with the

803 decrease of 6.7 days per decade reported by Wang et al. (2020a) just below the surface.

804   Regarding the timing of seasonal ground thaw, our results highlight that the increase in the duration

805 in the seasonal ground thaw (at 70 cm) is mostly driven by a progressive delay of the end date of the

806 thaw period. This result contrasts with those from Song et al. (2020) for the same period in the YRSR

807 who also modeled an increase of the seasonal thaw (at a 2 cm depth), although driven by an advancing

808 trend of the start date of the seasonal thaw.

809   Our warming trends at a 4 m depth for permafrost areas is 0.1 °C per decade, which is substantially

810 smaller than the 0.43 °C per decade observed at this depth between 1996 and 2006 in permafrost

811 boreholes along the Qinghai-Tibetan Highway in the North East of the QTP (Wu and Zhang, 2008).

812 Zhang et al. (2019) reported a 0.13 °C per decade of warming of the permafrost top during winter that

813 is consistent with the trend of 0.14 °C per decade we observe at 2 m depth (mean AL between 1.4 and

814 1.7 m in our simulations) for the months of December, January and February.

815   *5.2.2. Evaporation and runoff changes*

816   Our results are characterized by (i) an increase of both evaporation and runoff (Fig. 9A and 9B),

817 mainly driven by an increase in precipitation (Fig. 3 bottom), (ii) a runoff/(runoff+evaporation) ratio

exhibiting an increasing trend as a result of ground warming and permafrost disappearance that both enable more subsurface runoff along time (Fig. 9C and 10D) and (iii) an increase in the proportion of liquid water in the ground compared to ice (Fig. 9D). Regarding all these points, our results find a good consistency with the evolution reported by Gao et al. (2018) for the upper Heihe catchment (northeastern QTP) using a similar approach for a comparable period (1971-2013). The increasing trends in evaporation and runoff they report for the thawing season (dominant period for both processes) are comparable with the annual values we report: +10.0 mm per decade for evaporation (our study: +10.1 mm per decade) and +3.3 mm per decade for runoff (our study: +4.8 mm per decade). Similar evolutions are also reported by Wang and Gao (2022) for the Qinghai Lake catchment and by Qin et al. (2017) for the YRSR (1981-2015). These increases in runoff (especially surface runoff) are likely to have an influence on sediment transport. For instance, Li et al. (2021) showed that current precipitation augmentation over High Mountain Asia is driving a runoff increase, which contributes to a significant rise in fluvial sediment fluxes. Regarding differences, Qin et al. (2017) modeled a stronger evaporation increase (14.3 mm per decade) linked to a decreasing runoff coefficient. Similar to Li et al. (2019), we see that an important part of snow melt (49%) infiltrates the ground and later contributes to runoff and evaporation.

5.3. Evaporation vs runoff and sensitivity to climate conditions

Our results indicate that evaporation is particularly strong in the Paiku catchment. Over the 40 years of simulation, 10% of the total precipitation is converted into runoff, and the rest of the water is either directly returned to the atmosphere from the snowpack via snow sublimation or from the ground surface via evaporation. Comparatively, Gao et al. (2018) observed and modeled a ratio of around 35% for the Heihe catchment; Qin et al. (2017) reported an average ratio of 33% for the YRSR and Li et al. (2014), a ratio of 83% for the Qugaqie catchment (central QTP) but modeling hydrological fluxes only.

Our sensitivity test on evaporation and runoff for a slightly different climates (Sect. 4.4) highlights the fact that the role of permafrost regarding the runoff/evaporation distribution is a complex question,

843 as it has already been discussed in the literature (e.g. Bring et al., 2016). Some studies have suggested

844 that landscape-scale permafrost thaw would trigger more evaporation (Walvoord and Kurylyk, 2016).

845 This phenomenon was modeled by Wang et al. (2018) in the upper Heihe River Catchment, for which

846 they reported that the thickening of the active layer increased the ground storage capacity and led to a

847 decrease in runoff and an increase in evapotranspiration. Wang et al. (2020b) also reported that

848 permafrost thawing accelerated evapotranspiration (1961-2014).

849 Conversely, Zhang et al. (2003) and Carey and Woo (1999) reported that shallow frozen ground

850 conditions (such as a shallow active layer) maintain higher water contents close to the surface,

851 promoting higher evaporation. Sjöberg et al. (2021) modeled this phenomenon with a fully coupled

852 cryo-hydrological model including surface energy balance calculation. They modeled a slope with a

853 simplified geometry in 2D for different permafrost coverages. They found that hillslopes with

854 continuous permafrost have twice as high rates of evapotranspiration compared to hillslopes with no

855 permafrost.

856 As such, the interplay between the runoff/evaporation distribution and the ground thermal regime

857 in areas where permafrost coverage shows a spatiotemporal variability is difficult to apprehend (Fig

858 10). This complexity is most likely due to a strong sensitivity to the drainage conditions (fast flows of

859 steep mountain environments vs. slow flows of lowland catchments) and to the climate setting, both at

860 the annual scale (arid regions vs. wet regions) and at the seasonal time scale (relative timing of

861 temperature variations, rainfall, snowfall, snow melt and ground freeze/thaw).

862 Because it can both promote evaporation or runoff depending on the setting, the ground thermal

863 regime of the catchment seems to have the possibility to create a positive feedback, both towards lake

864 level decrease or increase. Further studies should therefore focus on comparing the thermo-hydrological

865 regime of different Tibetan catchments with contrasting lake level changes and permafrost coverage, to

866 test to which extent these differences can contribute to explain the spatial patterns of lake level changes

867 across the QTP.

6. Conclusion

We confirm that the Paiku catchment presents different types of ground cryological states from seasonally frozen ground to permafrost. Permafrost coverage shrinks from 27 to 22% of the land area of the catchment from the 1980s to the 2010s (19% loss of the 1980 permafrost area). The whole catchment warms up at a rate of 0.17 °C per decade (2 m deep), with a substantial elevation-dependent variability. This warming is concomitant with an increase in the duration of the seasonal thaw, mainly supported by a progressive delay of the end date of the thaw period. Where permafrost is present, active layer deepening is only observed where evaporation is relatively low (<150 mm yr^{-1}).

Over the simulation period, we also report an increase in evaporation (+10.1 mm per decade), surface and subsurface runoff (+1.3 and +3.5 mm per decade respectively). Together, this leads towards an increase of the runoff/(runoff + evaporation) ratio of +1.2% per decade. These results highlight the strong interdependence between the ground thermal and hydrological regimes and the necessity to jointly represent them to accurately quantify evaporation and runoff in this type of environment.

In regard of lake level variations, the results we present highlight that:

- The sum of the direct precipitation in the lake, the land runoff and the glacier runoff are not enough to compensate for the lake evaporation over the study period, hence driving the observed lake level decrease.

- Long-term hydrological trends in the catchment are led by trends in climate; and precipitation increase, jointly with glacier melt, provides enough water to drive a concomitant increase of runoff and evaporation.

- Ground thermal changes increase the distribution of liquid vs. frozen water in the ground and the duration of seasonal thaw, correlations suggest that these modifications increase evaporation. The warming of the ground is also related to the increase of subsurface runoff towards the lake.

- Ground warming and permafrost thawing promote subsurface runoff over time, contributing to an increase in the runoff/evaporation ratio of the catchment.

- Over the 40 years we studied, the presence of permafrost seems to promote evaporation at the expense of runoff. Yet this trend appears to be climate-dependent and the cryological state of the

895   ground might shift the runoff/evaporation distribution in the other direction under colder and wetter

896   climates.

897   At the scale of the QTP, these results have several implications. First, a better understanding of the

898   recent and future lake level variations will come with a better knowledge of spatial patterns and

899   temporal trends in precipitation. Second, climate changes are modifying the ground thermal regime of

900   Tibetan catchments through active layer deepening and changes in the seasonal freeze/thaw cycles,

901   affecting evaporation, runoff volumes and pathways and overall, changing the hydrological functioning

902   of Tibetan catchments (and the waterflow provided to the lakes). Finally, the effect of permafrost on

903   the distribution between evaporation and runoff seems to be dependent on the climate settings and the

904   permafrost coverage of the catchment. Further studies should investigate this phenomenon and how it

905   might contribute to explaining the contrasting lake level evolutions across the QTP.

Appendix A: model parameters

Table A1. Parameters of the model.

Depth	Layer	Parameter	Values	Source	Calculation
0.0 m	Surface	Albedo	0.24	Modis MCD43A3.006	November mean, 4600-5100 masl
		Emissivity	0.95	Modis MCD43A3.006	November mean, 4600-5100 masl
		Roughness	0.024	-	Adjusted to fit loggers T values
0.0 m	Top soil	Thickness	0.30 m	HiHydro Soil v1.0	modeling framework
		Porosity	0.5	Shangguann et al. 2013	mean
		Organic	8.60%	HiHydro Soil v1.0	catchment mean
		Mineral	41.40%	-	subtraction (100 - porosity - orga)
0.3 m		Soil type	Sand	Shangguann et al. 2013	dominant fraction
		Field capacity	0.32	HiHydro Soil v1.0	catchment mean
		Hydro cond	0.000030 m s^{-1}	HiHydro Soil v1.0	catchment mean
		Alpha	0.028 cm^{-1}	HiHydro Soil v1.0	catchment mean
0.3 m		n	1.481	HiHydro Soil v1.0	catchment mean
0.3 m	Bottom soil	Thickness	1.70 m	Shangguan et al. 2017	truncation, consistent with literature
		Porosity	0.4	Shangguann et al. 2013	catchment mean
		Organic	4.20%	HiHydro Soil v1.0	catchment mean
		Mineral	55.80%	-	subtraction (100 - porosity - orga)
1.7 m		Soil type	Sand	Shangguann et al. 2013	dominant fraction
		Field capacity	0.32	HiHydro Soil v1.0	catchment mean
		Hydro cond	0.000016 m s^{-1}	HiHydro Soil v1.0	catchment mean
		Alpha	0.062 cm^{-1}	HiHydro Soil v1.0	catchment mean
2.0 m		n	1.707	HiHydro Soil v1.0	catchment mean
2.0 m	Bedrock	Thickness	98.3 m	-	-
		Porosity	0.03	-	-
98 m		Organic	0%	-	-
		Mineral	97%	-	-
		Soil type	Sand	-	-
100 m		Field Capacity	0.03	-	equal to porosity

Appendix B: Geological map of the catchment
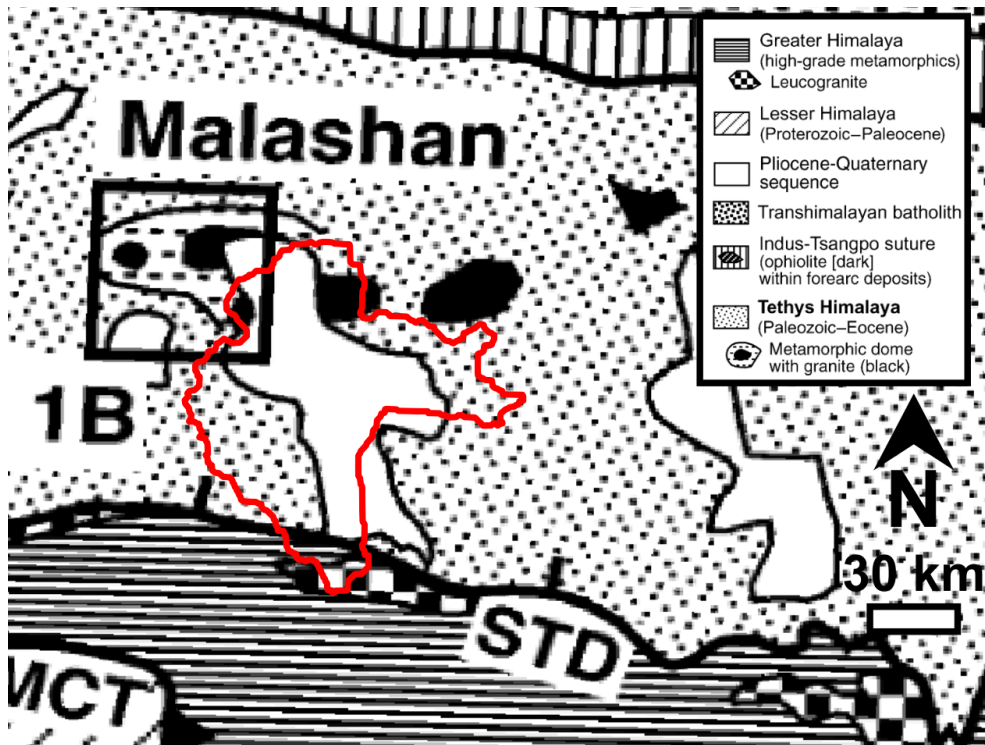
Figure B1. Geology of the catchment. Modified from Aoya et al. (2015). The red contour indicates the limits of the Paiku catchment.

Appendix C: TopoSUB subsampling of the catchment
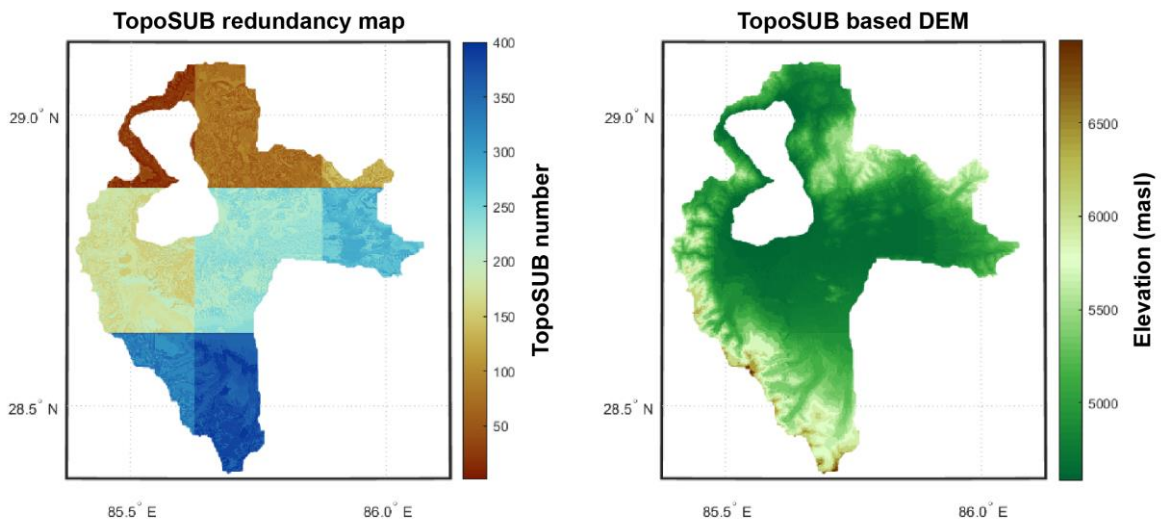
Figure C1. Application of the TopoSUB clustering method (Fiddes and Gruber, 2012) in the Paiku catchment. Left: number of the TopoSUB points. Strong color changes reflect the footprint of the 8 ERA5 pixels that the catchment intersects. Small color changes within a given of these zones show the distribution of the 50 TopoSUB points covering each tile (Sect. 3.2.2.) B: topographic map reconstructed using the TopoSUB approach.

Appendix D: Evaluation of forcing data
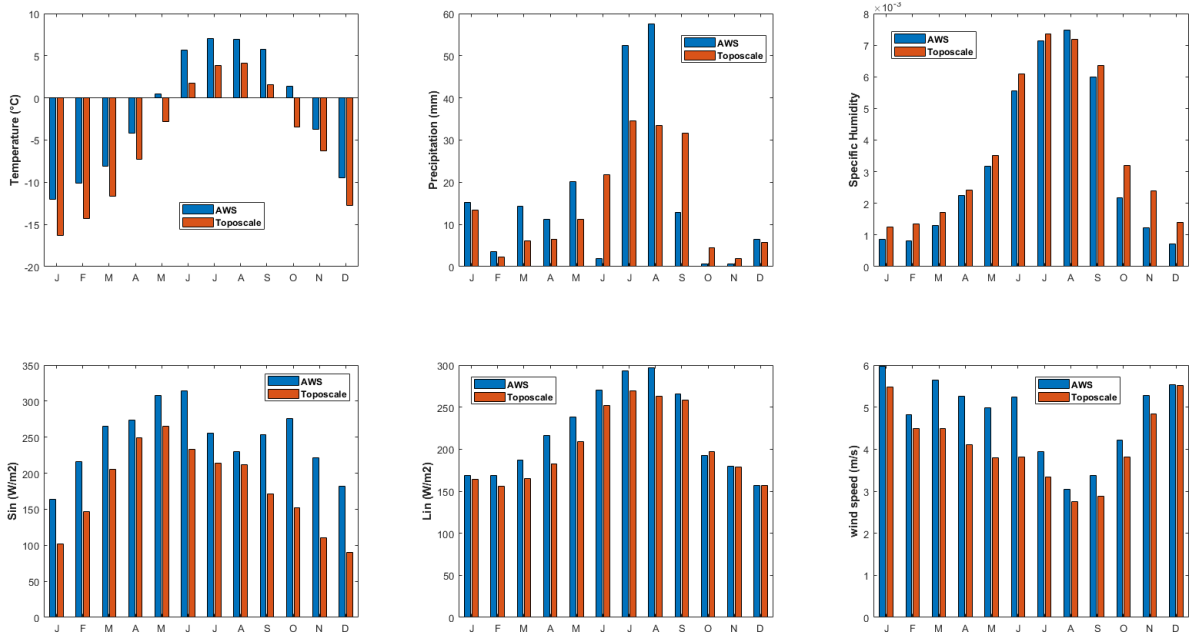
921
922 *Figure D1. Comparison between the AWS data and the model forcing data downscaled from ERA5 with*
923 *the TopoSCALE and TopoSUB approaches. Based on the AWS data, a monthly correction factor is*
924 *applied to the downscaled data so that monthly data matches for the observed period for each variable*
925 *(methodological details in Sect. 3.2.2.).*

Code availability. The CryoGrid community model (version 1.0) and related documentation are available at: https://github.com/CryoGrid/CryoGridCommunity_source.

Data availability. Field data have been saved on Zenodo.org and will be published with a DOI upon acceptance of the manuscript.

Author contribution. L.M, W. I. and S.W. designed the study. L.M. and M.M. conducted the numerical simulations. S.W., M.L. and L.M. contributed to the model development. F.B., W.I., Y.L. ad S.A. acquired field data. L.M., F.B., M.M., P.K., Y.L. and T.M. analyzed and processed the data. J.F. provided downscaled forcing data for the model. All authors contributed to result interpretation and to manuscript preparation.

Competing interests. The authors declare that they have no conflict of interest.

Acknowledgements. This study was funded by the open program of the Dutch Research Council (NWO) (ALWOP.467) and by the Strategic Priority Research Program of the Chinese Academy of Sciences within the Pan-Third Pole Environment framework (grant agreement no. XDA20100300). The land surface and lake simulations were performed on Utrecht Geosciences computer cluster. Sebastian Westermann acknowledges funding by European Space Agency Permafrost_CCI (https://climate.esa.int/en/projects/permafrost/). We are very grateful to the reviewers for their input which significantly improved this manuscript.

References

Almendinger, J. E.: Groundwater control of closed-basin lake levels under steady-state conditions, J Hydrol (Amst), 112, 293–318, https://doi.org/10.1016/0022-1694(90)90020-X, 1990.

Aoya, M., Wallis, S. R., Terada, K., Lee, J., Kawakami, T., Wang, Y., and Heizler, M.: North-south extension in the Tibetan crust triggered by granite emplacement, Geology, 33, 853, https://doi.org/10.1130/G21806.1, 2005.

Bhattacharya, A., Bolch, T., Mukherjee, K., King, O., Menounos, B., Kapitsa, V., Neckel, N., Yang, W., and Yao, T.: High Mountain Asian glacier response to climate revealed by multi-temporal satellite observations since the 1960s, Nat Commun, 12, 4133, https://doi.org/10.1038/s41467-021-24180-y, 2021.

Bibi, S., Wang, L., Li, X., Zhou, J., Chen, D., and Yao, T.: Climatic and associated cryospheric, biospheric, and hydrological changes on the Tibetan Plateau: a review, International Journal of Climatology, 38, e1–e17, https://doi.org/10.1002/joc.5411, 2018.

Biskop, S., Maussion, F., Krause, P., and Fink, M.: Differences in the water-balance components of four lakes in the southern-central Tibetan Plateau, Hydrol Earth Syst Sci, 20, 209–225, https://doi.org/10.5194/hess-20-209-2016, 2016.

Bolch, T., Shea, J. M., Liu, S., Azam, F. M., Gao, Y., Gruber, S., Immerzeel, W. W., Kulkarni, A., Li, H., Tahir, A. A., Zhang, G., and Zhang, Y.: Status and Change of the Cryosphere in the Extended Hindu Kush Himalaya Region, in: The Hindu Kush Himalaya Assessment: Mountains, Climate Change, Sustainability and People, edited by: Wester, P., Mishra, A., Mukherji, A., and Shrestha, A. B., Springer International Publishing, Cham, 209–255, https://doi.org/10.1007/978-3-319-92288-1_7, 2019.

Bring, A., Fedorova, I., Dibike, Y., Hinzman, L., Mård, J., Mernild, S. H., Prowse, T., Semenova, O., Stuefer, S. L., and Woo, M. -K.: Arctic terrestrial hydrology: A synthesis of processes, regional effects, and research challenges, J Geophys Res Biogeosci, 121, 621–649, https://doi.org/10.1002/2015JG003131, 2016.

Brun, F., Berthier, E., Wagnon, P., Kääb, A., and Treichler, D.: A spatially resolved estimate of High Mountain Asia glacier mass balances from 2000 to 2016, Nat Geosci, 10, 668–673, https://doi.org/10.1038/ngeo2999, 2017.

Brun, F., Treichler, D., Shean, D., and Immerzeel, W. W.: Limited Contribution of Glacier Mass Loss to the Recent Increase in Tibetan Plateau Lake Volume, Front Earth Sci (Lausanne), 8, 1–14, https://doi.org/10.3389/feart.2020.582060, 2020.

Cao, J., Qin, D., Kang, E., and Li, Y.: River discharge changes in the Qinghai-Tibet Plateau, Chinese Science Bulletin, 51, 594–600, https://doi.org/10.1007/s11434-006-0594-6, 2006.

Carey, S. K. and Woo, M.: Spatial variability of hillslope water balance, wolf creek basin, subarctic yukon, Hydrol Process, 15, 3113–3132, https://doi.org/10.1002/hyp.319, 2001.

Carey, S. K. and Woo, M.-K.: Hydrology of two slopes in subarctic Yukon, Canada, Hydrol Process, 13, 2549–2562, https://doi.org/10.1002/(SICI)1099-1085(199911)13:16<2549::AID-HYP938>3.0.CO;2-H, 1999.

Chen, R., Wang, G., Yang, Y., Liu, J., Han, C., Song, Y., Liu, Z., and Kang, E.: Effects of Cryospheric Change on Alpine Hydrology: Combining a Model With Observations in the Upper Reaches of the Hei River, China, Journal of Geophysical Research: Atmospheres, 123, 3414–3442, https://doi.org/10.1002/2017JD027876, 2018.

Cheng, G. and Jin, H.: Permafrost and groundwater on the Qinghai-Tibet Plateau and in northeast China, Hydrogeol J, 21, 5–23, https://doi.org/10.1007/s10040-012-0927-2, 2013.

Cuo, L., Zhang, Y., Bohn, T. J., Zhao, L., Li, J., Liu, Q., and Zhou, B.: Frozen soil degradation and its effects on surface hydrology in the northern Tibetan Plateau, Journal of Geophysical Research: Atmospheres, 120, 8276–8298, https://doi.org/10.1002/2015JD023193, 2015.

Dall'Amico, M., Endrizzi, S., Gruber, S., and Rigon, R.: A robust and energy-conserving model of freezing variably-saturated soil, Cryosphere, 5, 469–484, https://doi.org/10.5194/tc-5-469-2011, 2011.

Ding, Y., Zhang, S., Chen, R., Han, T., Han, H., Wu, J., Li, X., Zhao, Q., Shangguan, D., Yang, Y., Liu, J., Wang, S., Qin, J., and Chang, Y.: Hydrological Basis and Discipline System of Cryohydrology: From a Perspective of Cryospheric Science, Front Earth Sci (Lausanne), 8, 1–12, https://doi.org/10.3389/feart.2020.574707, 2020.

Fiddes, J. and Gruber, S.: TopoSUB: A tool for efficient large area numerical modelling in complex topography at sub-grid scales, Geosci Model Dev, 5, 1245–1257, https://doi.org/10.5194/gmd-5-1245-2012, 2012.

Fiddes, J. and Gruber, S.: TopoSCALE v.1.0: downscaling gridded climate data in complex terrain, Geosci Model Dev, 7, 387–405, https://doi.org/10.5194/gmd-7-387-2014, 2014.

Fisher, J. P., Estop-Aragonés, C., Thierry, A., Charman, D. J., Wolfe, S. A., Hartley, I. P., Murton, J. B., Williams, M., and Phoenix, G. K.: The influence of vegetation and soil characteristics on active-layer thickness of permafrost soils in boreal forest, Glob Chang Biol, 22, 3127–3140, https://doi.org/10.1111/gcb.13248, 2016.

Gao, B., Yang, D., Qin, Y., Wang, Y., Li, H., Zhang, Y., and Zhang, T.: Change in frozen soils and its effect on regional hydrology, upper Heihe basin, northeastern Qinghai-Tibetan Plateau, Cryosphere, 12, 657–673, https://doi.org/10.5194/tc-12-657-2018, 2018.

Gao, H., Hrachowitz, M., Fenicia, F., Gharari, S., and Savenije, H. H. G.: Testing the realism of a topography-driven model (FLEX-Topo) in the nested catchments of the Upper Heihe, China, Hydrol Earth Syst Sci, 18, 1895–1915, https://doi.org/10.5194/hess-18-1895-2014, 2014.

Gao, H., Wang, J., Yang, Y., Pan, X., Ding, Y., and Duan, Z.: Permafrost Hydrology of the Qinghai-Tibet Plateau: A Review of Processes and Modeling, Front Earth Sci (Lausanne), 8, 1–13, https://doi.org/10.3389/feart.2020.576838, 2021.

Gao, H., Han, C., Chen, R., Feng, Z., Wang, K., Fenicia, F., and Savenije, H.: Frozen soil hydrological modeling for a mountainous catchment northeast of the Qinghai–Tibet Plateau, Hydrol Earth Syst Sci, 26, 4187–4208, https://doi.org/10.5194/hess-26-4187-2022, 2022.

Gao, H., Fenicia, F., and Savenije, H. H. G.: HESS Opinions: Are soils overrated in hydrology?, https://doi.org/10.5194/egusphere-2023-125, n.d.

van Genuchten, M. Th.: A Closed-form Equation for Predicting the Hydraulic Conductivity of Unsaturated Soils, Soil Science Society of America Journal, 44, 892–898, https://doi.org/10.2136/sssaj1980.03615995004400050002x, 1980.

Hersbach, H., Bell, B., Berrisford, P., Hirahara, S., Horányi, A., Muñoz-Sabater, J., Nicolas, J., Peubey, C., Radu, R., Schepers, D., Simmons, A., Soci, C., Abdalla, S., Abellan, X., Balsamo, G., Bechtold, P., Biavati, G., Bidlot, J., Bonavita, M., Chiara, G., Dahlgren, P., Dee, D., Diamantakis, M., Dragani, R., Flemming, J., Forbes, R., Fuentes, M., Geer, A., Haimberger, L., Healy, S., Hogan, R. J., Hólm, E., Janisková, M., Keeley, S., Laloyaux, P., Lopez, P., Lupu, C., Radnoti, G., Rosnay, P., Rozum, I., Vamborg, F., Villaume, S., and Thépaut, J.: The ERA5 global reanalysis, Quarterly Journal of the Royal Meteorological Society, 146, 1999–2049, https://doi.org/10.1002/qj.3803, 2020.

Hu, G.-R., Li, X.-Y., and Yang, X.-F.: The impact of micro-topography on the interplay of critical zone architecture and hydrological processes at the hillslope scale: Integrated geophysical and hydrological experiments on the Qinghai-Tibet Plateau, J Hydrol (Amst), 583, 124618, https://doi.org/10.1016/j.jhydrol.2020.124618, 2020.

Huang, K., Dai, J., Wang, G., Chang, J., Lu, Y., Song, C., Hu, Z., Ahmed, N., and Ye, R.: The impact of land surface temperatures on suprapermafrost groundwater on the central Qinghai-Tibet Plateau, Hydrol Process, 34, 1475–1488, https://doi.org/10.1002/hyp.13677, 2020.

Hugonnet, R., McNabb, R., Berthier, E., Menounos, B., Nuth, C., Girod, L., Farinotti, D., Huss, M., Dussaillant, I., Brun, F., and Kääb, A.: Accelerated global glacier mass loss in the early twenty-first century, Nature, 592, 726–731, https://doi.org/10.1038/s41586-021-03436-z, 2021.

IPCC: IPCC Special Report on the Ocean and Cryosphere in a Changing Climate, Intergovernmental Panel on Climate Change, undefined, 2019.

Jiang, H., Yang, Y., Bai, Y., and Wang, H.: Evaluation of the Total, Direct, and Diffuse Solar Radiations From the ERA5 Reanalysis Data in China, IEEE Geoscience and Remote Sensing Letters, 17, 47–51, https://doi.org/10.1109/LGRS.2019.2916410, 2020.

Jiang, Q., Li, W., Fan, Z., He, X., Sun, W., Chen, S., Wen, J., Gao, J., and Wang, J.: Evaluation of the ERA5 reanalysis precipitation dataset over Chinese Mainland, J Hydrol (Amst), 595, 125660, https://doi.org/10.1016/j.jhydrol.2020.125660, 2021.

Jiao, D., Xu, N., Yang, F., and Xu, K.: Evaluation of spatial-temporal variation performance of ERA5 precipitation data in China, Sci Rep, 11, 17956, https://doi.org/10.1038/s41598-021-97432-y, 2021.

Kampf, S. K.: Variability and persistence of hillslope initial conditions: A continuous perspective on subsurface flow response to rain events, J Hydrol (Amst), 404, 176–185, https://doi.org/10.1016/j.jhydrol.2011.04.028, 2011.

Kelleners, T. J., Chandler, D. G., McNamara, J. P., Gribb, M. M., and Seyfried, M. S.: Modeling Runoff Generation in a Small Snow-Dominated Mountainous Catchment, Vadose Zone Journal, 9, 517–527, https://doi.org/10.2136/vzj2009.0033, 2010.

King, O., Bhattacharya, A., Bhambri, R., and Bolch, T.: Glacial lakes exacerbate Himalayan glacier mass loss, Sci Rep, 9, 18145, https://doi.org/10.1038/s41598-019-53733-x, 2019.

Koren, V., Schaake, J., Mitchell, K., Duan, Q.-Y., Chen, F., and Baker, J. M.: A parameterization of snowpack and frozen ground intended for NCEP weather and climate models, Journal of Geophysical Research: Atmospheres, 104, 19569–19585, https://doi.org/10.1029/1999JD900232, 1999.

Kurylyk, B. L., MacQuarrie, K. T. B., and McKenzie, J. M.: Climate change impacts on groundwater and soil temperatures in cold and temperate regions: Implications, mathematical theory, and emerging simulation tools, Earth Sci Rev, 138, 313–334, https://doi.org/10.1016/j.earscirev.2014.06.006, 2014.

Lamontagne-Hallé, P., McKenzie, J. M., Kurylyk, B. L., and Zipper, S. C.: Changing groundwater discharge dynamics in permafrost regions, Environmental Research Letters, 13, 084017, https://doi.org/10.1088/1748-9326/aad404, 2018.

Langer, M., Westermann, S., Boike, J., Kirillin, G., Grosse, G., Peng, S., and Krinner, G.: Rapid degradation of permafrost underneath waterbodies in tundra landscapes-Toward a representation of thermokarst in land surface models, J Geophys Res Earth Surf, 121, 2446–2470, https://doi.org/10.1002/2016JF003956, 2016.

Lei, Y., Yao, T., Bird, B. W., Yang, K., Zhai, J., and Sheng, Y.: Coherent lake growth on the central Tibetan Plateau since the 1970s: Characterization and attribution, J Hydrol (Amst), 483, 61–67, https://doi.org/10.1016/j.jhydrol.2013.01.003, 2013.

Lei, Y., Yang, K., Wang, B., Sheng, Y., Bird, B. W., Zhang, G., and Tian, L.: Response of inland lake dynamics over the Tibetan Plateau to climate change, Clim Change, 125, 281–290, https://doi.org/10.1007/s10584-014-1175-3, 2014.

Lei, Y., Yao, T., Yang, K., Bird, B. W., Tian, L., Zhang, X., Wang, W., Xiang, Y., Dai, Y., Lazhu, Zhou, J., and Wang, L.: An integrated investigation of lake storage and water level changes in the Paiku Co

basin, central Himalayas, J Hydrol (Amst), 562, 599–608, https://doi.org/10.1016/j.jhydrol.2018.05.040, 2018.

Lei, Y., Yao, T., Yang, K., Ma, Y., and Bird, B. W.: Contrasting hydrological and thermal intensities determine seasonal lake-level variations – a case study at Paiku Co on the southern Tibetan Plateau, Hydrol Earth Syst Sci, 25, 3163–3177, https://doi.org/10.5194/hess-25-3163-2021, 2021.

Lei, Y., Yang, K., Immerzeel, W. W., Song, P., Bird, B. W., He, J., Zhao, H., and Li, Z.: Critical Role of Groundwater Inflow in Sustaining Lake Water Balance on the Western Tibetan Plateau, Geophys Res Lett, 49, https://doi.org/10.1029/2022GL099268, 2022.

Li, B., Yu, Z., Liang, Z., and Acharya, K.: Hydrologic response of a high altitude glacierized basin in the central Tibetan Plateau, Glob Planet Change, 118, 69–84, https://doi.org/10.1016/j.gloplacha.2014.04.006, 2014.

Li, D., Lu, X., Overeem, I., Walling, D. E., Syvitski, J., Kettner, A. J., Bookhagen, B., Zhou, Y., and Zhang, T.: Exceptional increases in fluvial sediment fluxes in a warmer and wetter High Mountain Asia, Science (1979), 374, 599–603, https://doi.org/10.1126/science.abi9649, 2021.

Li, H., Li, X., Yang, D., Wang, J., Gao, B., Pan, X., Zhang, Y., and Hao, X.: Tracing Snowmelt Paths in an Integrated Hydrological Model for Understanding Seasonal Snowmelt Contribution at Basin Scale, Journal of Geophysical Research: Atmospheres, 124, 8874–8895, https://doi.org/10.1029/2019JD030760, 2019.

Liefert, D. T., Shuman, B. N., Parsekian, A. D., and Mercer, J. J.: Why Are Some Rocky Mountain Lakes Ephemeral?, Water Resour Res, 54, 5245–5263, https://doi.org/10.1029/2017WR022261, 2018.

Luo, D., Jin, H., Wu, Q., Bense, V. F., He, R., Ma, Q., Gao, S., Jin, X., and Lü, L.: Thermal regime of warm-dry permafrost in relation to ground surface temperature in the Source Areas of the Yangtze and Yellow rivers on the Qinghai-Tibet Plateau, SW China, Science of the Total Environment, 618, 1033–1045, https://doi.org/10.1016/j.scitotenv.2017.09.083, 2018.

Luo, D., Jin, H., Bense, V. F., Jin, X., and Li, X.: Hydrothermal processes of near-surface warm permafrost in response to strong precipitation events in the Headwater Area of the Yellow River, Tibetan Plateau, Geoderma, 376, 114531, https://doi.org/10.1016/j.geoderma.2020.114531, 2020.

Magnin, F., Josnin, J.-Y., Ravanel, L., Pergaud, J., Pohl, B., and Deline, P.: Modelling rock wall permafrost degradation in the Mont Blanc massif from the LIA to the end of the 21st century, Cryosphere, 11, 1813–1834, https://doi.org/10.5194/tc-11-1813-2017, 2017.

Martin, L. C. P., Nitzbon, J., Aas, K. S. S., Etzelmüller, B., Kristiansen, H., and Westermann, S.: Stability Conditions of Peat Plateaus and Palsas in Northern Norway, J Geophys Res Earth Surf, 124, 705–719, https://doi.org/10.1029/2018JF004945, 2019.

Maurer, J. M., Schaefer, J. M., Rupper, S., and Corley, A.: Acceleration of ice loss across the Himalayas over the past 40 years, Sci Adv, 5, https://doi.org/10.1126/sciadv.aav7266, 2019.

McDonnell, J. J.: Are all runoff processes the same?, Hydrol Process, 27, 4103–4111, https://doi.org/10.1002/hyp.10076, 2013.

Mirus, B. B. and Loague, K.: How runoff begins (and ends): Characterizing hydrologic response at the catchment scale, Water Resour Res, 49, 2987–3006, https://doi.org/10.1002/wrcr.20218, 2013.

Monin, A. S. and Obukhov, A. M.: Basic laws of turbulent mixing in the surface layer of the atmosphere, Contrib. Geophys. Inst. Acad. Sci. USSR, 151, 163–187, 1954.

Mualem, Y.: A new model for predicting the hydraulic conductivity of unsaturated porous media, Water Resour Res, 12, 513–522, https://doi.org/10.1029/WR012i003p00513, 1976.

Nakano, Y. and Brown, J.: Mathematical Modeling and Validation of the Thermal Regimes in Tundra Soils, Barrow, Alaska, Arctic and Alpine Research, 4, 19, https://doi.org/10.2307/1550211, 1972.

Niu, L., Ye, B., Li, J., and Sheng, Y.: Effect of permafrost degradation on hydrological processes in typical basins with various permafrost coverage in Western China, Sci China Earth Sci, 54, 615–624, https://doi.org/10.1007/s11430-010-4073-1, 2011.

Niu, L., Ye, B., Ding, Y., Li, J., Zhang, Y., Sheng, Y., and Yue, G.: Response of hydrological processes to permafrost degradation from 1980 to 2009 in the Upper Yellow River Basin, China, Hydrology Research, 47, 1014–1024, https://doi.org/10.2166/nh.2016.096, 2016.

Obu, J., Westermann, S., Bartsch, A., Berdnikov, N., Christiansen, H. H., Dashtseren, A., Delaloye, R., Elberling, B., Etzelmüller, B., Kholodov, A., Khomutov, A., Kääb, A., Leibman, M. O., Lewkowicz, A. G., Panda, S. K., Romanovsky, V., Way, R. G., Westergaard-Nielsen, A., Wu, T., Yamkhin, J., and Zou, D.: Northern Hemisphere permafrost map based on TTOP modelling for 2000–2016 at 1 km2 scale, Earth Sci Rev, 193, 299–316, https://doi.org/10.1016/j.earscirev.2019.04.023, 2019.

Orsolini, Y., Wegmann, M., Dutra, E., Liu, B., Balsamo, G., Yang, K., de Rosnay, P., Zhu, C., Wang, W., Senan, R., and Arduini, G.: Evaluation of snow depth and snow cover over the Tibetan Plateau in global reanalyses using in situ and satellite remote sensing observations, Cryosphere, 13, 2221–2239, https://doi.org/10.5194/tc-13-2221-2019, 2019.

Penman, H. L.: Natural evaporation from open water, bare soil and grass, Proc R Soc Lond A Math Phys Sci, 193, 120–145, 1948.

Pepin, N., Bradley, R. S., Diaz, H. F., Baraer, M., Caceres, E. B., Forsythe, N., Fowler, H., Greenwood, G., Hashmi, M. Z., Liu, X. D., Miller, J. R., Ning, L., Ohmura, A., Palazzi, E., Rangwala, I., Schöner, W., Severskiy, I., Shahgedanova, M., Wang, M. B., Williamson, S. N., and Yang, D. Q.: Elevation-dependent warming in mountain regions of the world, Nat Clim Chang, 5, 424–430, https://doi.org/10.1038/nclimate2563, 2015.

Pomeroy, J. W., Gray, D. M., Brown, T., Hedstrom, N. R., Quinton, W. L., Granger, R. J., and Carey, S. K.: The cold regions hydrological model: a platform for basing process representation and model structure on physical evidence, Hydrol Process, 21, 2650–2667, https://doi.org/10.1002/hyp.6787, 2007.

Qiao, B., Zhu, L., and Yang, R.: Temporal-spatial differences in lake water storage changes and their links to climate change throughout the Tibetan Plateau, Remote Sens Environ, 222, 232–243, https://doi.org/10.1016/j.rse.2018.12.037, 2019.

Qin, Y., Yang, D., Gao, B., Wang, T., Chen, J., Chen, Y., Wang, Y., and Zheng, G.: Impacts of climate warming on the frozen ground and eco-hydrology in the Yellow River source region, China, Science of the Total Environment, 605–606, 830–841, https://doi.org/10.1016/j.scitotenv.2017.06.188, 2017.

Qin, Y., Chen, J., Yang, D., and Wang, T.: Estimating Seasonally Frozen Ground Depth From Historical Climate Data and Site Measurements Using a Bayesian Model, Water Resour Res, 54, 4361–4375, https://doi.org/10.1029/2017WR022185, 2018.

Qin, Y., Wu, T., Zhang, P., Liu, W., Xue, S., and Guo, Z.: Spatiotemporal freeze–thaw variations over the Qinghai- Tibet Plateau 1981–2017 from reanalysis, International Journal of Climatology, 41, 1438–1454, https://doi.org/10.1002/joc.6849, 2021.

Ran, Y., Li, X., and Cheng, G.: Climate warming over the past half century has led to thermal degradation of permafrost on the Qinghai–Tibet Plateau, Cryosphere, 12, 595–608, https://doi.org/10.5194/tc-12-595-2018, 2018.

RGI Consortium: Randolph Glacier Inventory - A Dataset of Global Glacier Outlines, Version 6, 2017.

Richards, L. A.: CAPILLARY CONDUCTION OF LIQUIDS THROUGH POROUS MEDIUMS, Physics (College Park Md), 1, 318–333, https://doi.org/10.1063/1.1745010, 1931.

Richardson, L. F.: Weather Prediction by Numerical Process, Cambridge University Press, 1922.

Rosenberry, D. O., Lewandowski, J., Meinikmann, K., and Nützmann, G.: Groundwater - the disregarded component in lake water and nutrient budgets. Part 1: effects of groundwater on hydrology, Hydrol Process, 29, 2895–2921, https://doi.org/10.1002/hyp.10403, 2015.

Samuel, J. M., Sivapalan, M., and Struthers, I.: Diagnostic analysis of water balance variability: A comparative modeling study of catchments in Perth, Newcastle, and Darwin, Australia, Water Resour Res, 44, https://doi.org/10.1029/2007WR006694, 2008.

Savenije, H. H. G.: HESS opinions "topography driven conceptual modelling (FLEX-Topo)," Hydrol Earth Syst Sci, 14, 2681–2692, https://doi.org/10.5194/hess-14-2681-2010, 2010.

Searle, M. P., Parrish, R. R., Hodges, K. V., Hurford, A., Ayres, M. W., and Whitehouse, M. J.: Shisha Pangma Leucogranite, South Tibetan Himalaya: Field Relations, Geochemistry, Age, Origin, and Emplacement, J Geol, 105, 295–318, https://doi.org/10.1086/515924, 1997.

Seibert, J., Rodhe, A., and Bishop, K.: Simulating interactions between saturated and unsaturated storage in a conceptual runoff model, Hydrol Process, 17, 379–390, https://doi.org/10.1002/hyp.1130, 2003.

Shaman, J., Stieglitz, M., Engel, V., Koster, R., and Stark, C.: Representation of subsurface storm flow and a more responsive water table in a TOPMODEL-based hydrology model, Water Resour Res, 38, 31-1-31–16, https://doi.org/10.1029/2001wr000636, 2002.

Shangguan, W., Dai, Y., Liu, B., Zhu, A., Duan, Q., Wu, L., Ji, D., Ye, A., Yuan, H., Zhang, Q., Chen, D., Chen, M., Chu, J., Dou, Y., Guo, J., Li, H., Li, J., Liang, L., Liang, X., Liu, H., Liu, S., Miao, C., and Zhang, Y.: A China data set of soil properties for land surface modeling, J Adv Model Earth Syst, 5, 212–224, https://doi.org/10.1002/jame.20026, 2013.

Shangguan, W., Hengl, T., Mendes de Jesus, J., Yuan, H., and Dai, Y.: Mapping the global depth to bedrock for land surface modeling, J Adv Model Earth Syst, 9, 65–88, https://doi.org/10.1002/2016MS000686, 2017.

Shean, D. E., Bhushan, S., Montesano, P., Rounce, D. R., Arendt, A., and Osmanoglu, B.: A Systematic, Regional Assessment of High Mountain Asia Glacier Mass Balance, Front Earth Sci (Lausanne), 7, 1–19, https://doi.org/10.3389/feart.2019.00363, 2020.

Sjöberg, Y., Jan, A., Painter, S. L., Coon, E. T., Carey, M. P., O'Donnell, J. A., and Koch, J. C.: Permafrost Promotes Shallow Groundwater Flow and Warmer Headwater Streams, Water Resour Res, 57, 1–20, https://doi.org/10.1029/2020WR027463, 2021.

Song, L., Wang, L., Li, X., Zhou, J., Luo, D., Jin, H., Qi, J., Zeng, T., and Yin, Y.: Improving Permafrost Physics in a Distributed Cryosphere-Hydrology Model and Its Evaluations at the Upper Yellow River Basin, Journal of Geophysical Research: Atmospheres, 125, 1–22, https://doi.org/10.1029/2020JD032916, 2020.

Themeßl, M. J., Gobiet, A., and Leuprecht, A.: Empirical-statistical downscaling and error correction of daily precipitation from regional climate models, International Journal of Climatology, 31, 1530–1544, https://doi.org/10.1002/joc.2168, 2011.

Vionnet, V., Brun, E., Morin, S., Boone, A., Faroux, S., Le Moigne, P., Martin, E., and Willemet, J.-M.: The detailed snowpack scheme Crocus and its implementation in SURFEX v7.2, Geosci Model Dev, 5, 773–791, https://doi.org/10.5194/gmd-5-773-2012, 2012.

Vörösmarty, C. J., Moore, B., Grace, A. L., Gildea, M. P., Melillo, J. M., Peterson, B. J., Rastetter, E. B., and Steudler, P. A.: Continental scale models of water balance and fluvial transport: An application to South America, Global Biogeochem Cycles, 3, 241–265, https://doi.org/10.1029/GB003i003p00241, 1989.

Walvoord, M. A. and Kurylyk, B. L.: Hydrologic Impacts of Thawing Permafrost—A Review, Vadose Zone Journal, 15, 0, https://doi.org/10.2136/vzj2016.01.0010, 2016.

Wang, C., Zhao, W., and Cui, Y.: Changes in the Seasonally Frozen Ground Over the Eastern Qinghai-Tibet Plateau in the Past 60 Years Characteristics of Seasonally Frozen, 8, 1–11, https://doi.org/10.3389/feart.2020.00270, 2020a.

Wang, G., Li, Y., Hu, H., and Wang, Y.: Synergistic effect of vegetation and air temperature changes on soil water content in alpine frost meadow soil in the permafrost region of Qinghai-Tibet, Hydrol Process, 22, 3310–3320, https://doi.org/10.1002/hyp.6913, 2008.

Wang, G., Lin, S., Hu, Z., Lu, Y., Sun, X., and Huang, K.: Improving Actual Evapotranspiration Estimation Integrating Energy Consumption for Ice Phase Change Across the Tibetan Plateau, Journal of Geophysical Research: Atmospheres, 125, 1–13, https://doi.org/10.1029/2019JD031799, 2020b.

Wang, L., Yi, C., Xu, X., Schütt, B., Liu, K., and Zhou, L.: Soil properties in two soil profiles from terraces of the Nam Co Lake in Tibet, China, J Mt Sci, 6, 354–361, https://doi.org/10.1007/s11629-009-1017-3, 2009.

Wang, Q., Fan, X., and Wang, M.: Recent warming amplification over high elevation regions across the globe, Clim Dyn, 43, 87–101, https://doi.org/10.1007/s00382-013-1889-3, 2014.

Wang, X. and Gao, B.: Frozen soil change and its impact on hydrological processes in the Qinghai Lake Basin, the Qinghai-Tibetan Plateau, China, J Hydrol Reg Stud, 39, 100993, https://doi.org/10.1016/j.ejrh.2022.100993, 2022.

Wang, Y., Yang, H., Gao, B., Wang, T., Qin, Y., and Yang, D.: Frozen ground degradation may reduce future runoff in the headwaters of an inland river on the northeastern Tibetan Plateau, J Hydrol (Amst), 564, 1153–1164, https://doi.org/10.1016/j.jhydrol.2018.07.078, 2018.

Watras, C. J., Read, J. S., Holman, K. D., Liu, Z., Song, Y.-Y., Watras, A. J., Morgan, S., and Stanley, E. H.: Decadal oscillation of lakes and aquifers in the upper Great Lakes region of North America: Hydroclimatic implications, Geophys Res Lett, 41, 456–462, https://doi.org/10.1002/2013GL058679, 2014.

Westermann, S., Schuler, T. V., Gisnås, K., and Etzelmüller, B.: Transient thermal modeling of permafrost conditions in Southern Norway, Cryosphere, 7, 719–739, https://doi.org/10.5194/tc-7-719-2013, 2013.

Westermann, S., Langer, M., Boike, J., Heikenfeld, M., Peter, M., Etzelmüller, B., and Krinner, G.: Simulating the thermal regime and thaw processes of ice-rich permafrost ground with the land-surface model CryoGrid 3, Geosci Model Dev, 9, 523–546, https://doi.org/10.5194/gmd-9-523-2016, 2016.

Westermann, S., Ingeman-Nielsen, T., Scheer, J., Aalstad, K., Aga, J., Chaudhary, N., Etzelmüller, B., Filhol, S., Kääb, A., Renette, C., Schmidt, L. S., Schuler, T. V., Zweigel, R. B., Martin, L., Morard, S., Ben-Asher, M., Angelopoulos, M., Boike, J., Groenke, B., Miesner, F., Nitzbon, J., Overduin, P., Stuenzi, S. M., and Langer, M.: The CryoGrid community model (version 1.0) – a multi-physics toolbox for climate-driven simulations in the terrestrial cryosphere, Geosci Model Dev, 16, 2607–2647, https://doi.org/10.5194/gmd-16-2607-2023, 2023.

Wu, Q. and Zhang, T.: Recent permafrost warming on the Qinghai-Tibetan Plateau, J Geophys Res, 113, D13108, https://doi.org/10.1029/2007JD009539, 2008.

Wünnemann, B., Yan, D., and Ci, R.: Morphodynamics and lake level variations at Paiku Co, southern Tibetan Plateau, China, Geomorphology, 246, 489–501, https://doi.org/10.1016/j.geomorph.2015.07.007, 2015.

Yang, K., Wu, H., Qin, J., Lin, C., Tang, W., and Chen, Y.: Recent climate changes over the Tibetan Plateau and their impacts on energy and water cycle: A review, Glob Planet Change, 112, 79–91, https://doi.org/10.1016/j.gloplacha.2013.12.001, 2014a.

Yang, K., Wang, J., Lei, Y., Chen, Y., Zhu, L., Ding, B., and Qin, J.: Quantifying evaporation and its decadal change for Lake Nam Co, central Tibetan Plateau, Journal of Geophysical Research: Atmospheres, 121, 7578–7591, https://doi.org/10.1002/2015JD024523, 2016.

Yang, S., Zhang, H., Kong, M., Liu, Y., Liu, H., and Xu, R.: Study on surficial soil geochemistry in the high-elevation and -frigid mountainous region: A case of Qulong porphyry copper deposit in Tibet, J Geochem Explor, 139, 144–151, https://doi.org/10.1016/j.gexplo.2013.06.001, 2014b.

Yang, Y., Wu, Q., Jin, H., Wang, Q., Huang, Y., Luo, D., Gao, S., and Jin, X.: Delineating the hydrological processes and hydraulic connectivities under permafrost degradation on Northeastern Qinghai-Tibet Plateau, China, J Hydrol (Amst), 569, 359–372, https://doi.org/10.1016/j.jhydrol.2018.11.068, 2019.

Yao, F., Wang, J., Yang, K., Wang, C., Walter, B. A., and Crétaux, J.-F.: Lake storage variation on the endorheic Tibetan Plateau and its attribution to climate change since the new millennium, Environmental Research Letters, 13, 064011, https://doi.org/10.1088/1748-9326/aab5d3, 2018.

Yechieli, Y., Ronen, D., Berkowitz, B., Dershowitz, W. S., and Hadad, A.: Aquifer Characteristics Derived From the Interaction Between Water Levels of a Terminal Lake (Dead Sea) and an Adjacent Aquifer, Water Resour Res, 31, 893–902, https://doi.org/10.1029/94WR03154, 1995.

Yi, S., Arain, M. A., and Woo, M.-K.: Modifications of a land surface scheme for improved simulation of ground freeze-thaw in northern environments, Geophys Res Lett, 33, L13501, https://doi.org/10.1029/2006GL026340, 2006.

Yuan, Z., Jin, H., Wang, Q., Wu, Q., Li, G., Jin, X., and Ma, Q.: Profile distributions of soil organic carbon fractions in a permafrost region of the Qinghai–Tibet Plateau, Permafr Periglac Process, 31, 538–547, https://doi.org/10.1002/ppp.2055, 2020.

Zhang, G., Yao, T., Piao, S., Bolch, T., Xie, H., Chen, D., Gao, Y., O'Reilly, C. M., Shum, C. K., Yang, K., Yi, S., Lei, Y., Wang, W., He, Y., Shang, K., Yang, X., and Zhang, H.: Extensive and drastically different alpine lake changes on Asia's high plateaus during the past four decades, Geophys Res Lett, 44, 252–260, https://doi.org/10.1002/2016GL072033, 2017.

Zhang, G., Nan, Z., Wu, X., Ji, H., and Zhao, S.: The Role of Winter Warming in Permafrost Change Over the Qinghai-Tibet Plateau, Geophys Res Lett, 46, 11261–11269, https://doi.org/10.1029/2019GL084292, 2019.

Zhang, G., Yao, T., Xie, H., Yang, K., Zhu, L., Shum, C. K., Bolch, T., Yi, S., Allen, S., Jiang, L., Chen, W., and Ke, C.: Response of Tibetan Plateau lakes to climate change: Trends, patterns, and mechanisms, Earth Sci Rev, 208, 103269, https://doi.org/10.1016/j.earscirev.2020.103269, 2020a.

Zhang, G., Bolch, T., Chen, W., and Crétaux, J.-F.: Comprehensive estimation of lake volume changes on the Tibetan Plateau during 1976–2019 and basin-wide glacier contribution, Science of The Total Environment, 772, 145463, https://doi.org/10.1016/j.scitotenv.2021.145463, 2021a.

Zhang, G., Nan, Z., Zhao, L., Liang, Y., and Cheng, G.: Qinghai-Tibet Plateau wetting reduces permafrost thermal responses to climate warming, Earth Planet Sci Lett, 562, 116858, https://doi.org/10.1016/j.epsl.2021.116858, 2021b.

Zhang, H., Immerzeel, W. W., Zhang, F., de Kok, R. J., Chen, D., and Yan, W.: Snow cover persistence reverses the altitudinal patterns of warming above and below 5000 m on the Tibetan Plateau, Science of The Total Environment, 803, 149889, https://doi.org/10.1016/j.scitotenv.2021.149889, 2022.

Zhang, X., Wang, R., Yao, Z., and Liu, Z.: Variations in glacier volume and snow cover and their impact on lake storage in the Paiku Co Basin, in the Central Himalayas, Hydrol Process, 34, 1920–1933, https://doi.org/10.1002/hyp.13703, 2020b.

Zhang, Y., Ohata, T., and Kadota, T.: Land-surface hydrological processes in the permafrost region of the eastern Tibetan Plateau, J Hydrol (Amst), 283, 41–56, https://doi.org/10.1016/S0022-1694(03)00240-3, 2003.

Zhong, X., Wang, L., Zhou, J., Li, X., Qi, J., Song, L., and Wang, Y.: Precipitation Dominates Long-Term Water Storage Changes in Nam Co Lake (Tibetan Plateau) Accompanied by Intensified Cryosphere

Melts Revealed by a Basin-Wide Hydrological Modelling, Remote Sens (Basel), 12, 1926, https://doi.org/10.3390/rs12121926, 2020.

Zhou, J., Wang, L., Zhang, Y., Guo, Y., Li, X., and Liu, W.: Exploring the water storage changes in the largest lake (Selin Co) over the Tibetan Plateau during 2003–2012 from a basin-wide hydrological modeling, Water Resour Res, 51, 8060–8086, https://doi.org/10.1002/2014WR015846, 2015.

Zou, D., Zhao, L., Sheng, Y., Chen, J., Hu, G., Wu, T., Wu, J., Xie, C., Wu, X., Pang, Q., Wang, W., Du, E., Li, W., Liu, G., Li, J., Qin, Y., Qiao, Y., Wang, Z., Shi, J., and Cheng, G.: A new map of permafrost distribution on the Tibetan Plateau, Cryosphere, 11, 2527–2542, https://doi.org/10.5194/tc-11-2527-2017, 2017.

Zweigel, R. B., Westermann, S., Nitzbon, J., Langer, M., Boike, J., Etzelmüller, B., and Vikhamar Schuler, T.: Simulating Snow Redistribution and its Effect on Ground Surface Temperature at a High-Arctic Site on Svalbard, J Geophys Res Earth Surf, 126, 1–21, https://doi.org/10.1029/2020JF005673, 2021.